COMPREHENSIVE APPROACH TO ENHANCE PEROVSKITE SOLAR CELLS EFFICIENCY AND STABILITY THROUGH CHARGE TRANSPORT AND INTERLAYER MODIFICATIONS

by

Merlan Nurzhanov

A thesis

presented to the University of Waterloo

in fulfillment of the

thesis requirement for the degree of

Master of Applied Science

in

Chemical Engineering (Nanotechnology)

Waterloo, Ontario, Canada, 2022

Author's Declaration

I hereby declare that I am the sole author of this thesis. This is a true copy of the thesis, including any required final revisions, as accepted by my examiners. I understand that my thesis may be made electronically available to the public.

Abstract

Perovskite solar cells (PSCs) having numerous advantages for photovoltaic applications, such as high absorption coefficient, tunable bandgap, high crystallinity and long carrier diffusion length, attracted significant interest in the academic field in the recent decade. However, due to significant constraints in its fabrication, the perovskite solar cells field is still in its research and development stage. Generally, the commercial prospects of photovoltaic technology depend on cost, efficiency and stability. Perovskite solar cells are projected to be low-cost because they require small amounts of cheap materials and low production costs. However, even though power conversion efficiency has soared in the past decade, the stability of these cells still needs to improve to provide long-term viability. In this work, I employed passivation and compositional modification methods to improve charge transport and interfacial layers in the perovskite solar cells to enhance the efficiency and operation stability of perovskite solar cells. This work is divided into four chapters. In the first chapter, I discuss the fundamentals and recent challenges of the perovskite solar cell field; in the second and third chapters I introduce my research work, and in the last fourth chapter, I provide a summary and future work.

In the second chapter, my research work is focused on the incorporation of a small organic molecule called EGTA (ethylene glycol-bis (β-aminoethyl ether)-*N, N, N, N* -tetraacetic acid) into the SnO_2 colloidal solution. The formation of a complex with SnO_2 allowed the EGTA-SnO_2-based electron transport layer (ETL) devices to achieve an efficiency of 21.14% while maintaining good reproducibility under low-temperature manufacturing conditions. In addition, the EGTA-treated SnO_2 solution demonstrates better surface coverage and improved electron mobility compared to the untreated SnO_2-based ETL. At the same time, the number of defects at the interface between the ETL and perovskite layers was reduced, which resulted in the devices exhibiting negligible hysteresis. Unencapsulated EGTA-SnO_2-based devices displayed improved stability under ambient settings, keeping more than 80% of their original efficiency over 500 h.

In the third chapter, we used three distinct isomers of dicyanobenzene (DCB): ortho, meta, and para, as a passivation compound between the perovskite and the Spiro-OMeTAD hole transport layer. The meta-dicyano isomer significantly reduced the amount of unreacted lead iodide. PSCs

that were passivated with 1,3-DCB increased PCE from 18.25% to 21.07%, reduced hysteresis and retains over 80% efficiency over 1000 h under ambient conditions. The performance improvement is related to the effective passivation of both shallow and deep charge traps. This work sheds some light on the impact of isomerism in the passivation of perovskite films and suggests a feasible approach to improving the performance of PSCs by using small organic compounds with two –CN functional groups.

The final chapter summarizes the main findings of this work and suggests some future directions.

Acknowledgements

I thank my supervisor, Professor Yuning Li, who gave me tremendous help and directed me on my research path. His enormous help in planning and arranging the research work and insightful advice allowed me to produce this work.

I would like to thank Yaoyao Li for guiding me throughout the process of synthesizing and fabricating Perovskite Solar Cells. Many thanks to Professor Vivek Maheshwari for the guidance he provided. I owe great gratitude to Yi Yuan, Avi Mathur, Daniel Afzal, and Zhe Huang, who instructed and helped me test fabricated electronic devices. Many thanks go to Xiguang Gao and Jenner Ngai for their invaluable assistance. Additionally, I would like to extend my gratitude to Charles Del Castel, who gave an enormous help in using AFM and FTIR measurements.

In conclusion, I would like to express my gratitude to all of my family members and friends who have been there for me throughout the difficult times that have occurred over the past two years and to others at the University of Waterloo, who have been very helpful to me in both my day-to-day life and my scientific research.

Table of Contents

List of Figures

List of Tables

List of Abbreviations

AFM: Atomic Force Microscopy

DMF: N, N – Dimethylmethanamide

DMSO: Dimethyl sulfoxide

EDTA: Ethylenediaminetetraacetic acid

EGTA: Ethylene glycol-bis(β-aminoethyl ether)-*N*, *N*, *N′, N′*-tetraacetic acid

ETL: Electron transporting layer

FA: Formamidinium

FF: Fill Factor

FTO: Fluorine-doped Tin Oxide glass

HTL: Hole transporting layer

I-V: Current-voltage

ITO: Indium tin oxide

J-V: Current density-voltage

J_{SC}: Short-Circuit Current Density

MA: Methylammonium

$MAPbI_3$: Methylammonium lead triiodide

$MAPbBr_3$: Methylammonium lead tribromide

OIHP: Organic-inorganic hybrid perovskites

OPV: Organic Photovoltaic

OSC: Organic Solar Cell

PCBM: [6,6]-phenyl-C61-butyric acid methyl ester

PCE: Power conversion efficiency

PEDOT:PSS: Poly(3,4-ethylenedioxythiophene) polystyrene sulfonate

PSC: Perovskite Solar Cell

PTAA: Poly (triaryl amine)

PV: Photovoltaic

RMS: Root Mean Square

SEM: Scanning electron microscopy

Si: Silicon

UV-Vis: Ultraviolet-Visible

V_{OC}: Open-Circuit Voltage

XRD: X-ray Diffraction

Other abbreviations and symbols are defined in the text.

CHAPTER 1. INTRODUCTION

1.1. Climate change, renewable energy, and solar cell technology

Climate change is one of the main challenges of our time. The consequences of the rise in global temperature are the unpredictability of weather conditions, which threatens food production, and sea-level elevation, which increases the risk of natural disasters at an unprecedented scale. In addition, rapid industrialization, large-scale deforestation and the universal use of non-renewable energy sources such as oil and gas have increased greenhouse gas emissions into the atmosphere.

The world is on the verge of an unprecedented turning point. To mitigate the consequences of climate change, we must reduce the consumption of these carbon-saturated fuels. For this, renewable energy sources are considered a centrepiece of this plan.

An increase in energy use from renewable sources can bring other positive outcomes, including economic impact. For example, using such technologies makes it possible to create jobs and reduce air pollution at the local level and water consumption. In addition, renewable energy production technologies can be based on local resources and, therefore, help protect countries' economies from external shocks related to energy security. Thus, this type of energy will become not only environmentally friendly but also an economically profitable way of generating power.

The advantages of renewable energy sources are numerous, but the obstacles to their implementation are just as significant to address. For example, the prevailing market structures, lack of understanding of the principles of operation of new technologies based on renewable energy sources, demanding access to financing and its high cost, small market capacity, and political uncertainty — all these factors have played a role in curbing the use of renewable energy sources.

Despite these issues, the demand for cheaper and greener electricity is growing more than at any other time in history. This is especially true for solar energy and batteries. As a result, the overall

cost of these technologies has declined at an unprecedented rate over the past decade, and energy-efficient alternatives such as LED lighting have also expanded.

However, current solar energy technologies in silicon (Si) solar cells do not give the needed result: Si-based solar cells soon reach the limits of efficiency and cost. The potential for a future reduction in the price of electricity from Si solar cells is limited. Making each cell requires a fair amount of energy and expenses to build. Although the cost of production can be slightly compressed, the prices of a solar installation are now dominated by additional costs — installation, wiring, electronics, and maintenance.

By the beginning of the new millennium, alternative solar cells based on perovskites began to develop very rapidly. Perovskite solar cells (PSCs) are a new generation of devices that convert sunlight energy into electricity. Currently, the efficiency of such devices is catching up with the record values of the most common polycrystalline silicon-based solar cells today.

1.2. Perovskite solar cells

The basis of a perovskite solar cell is a thin layer of crystalline light-absorbing material — hybrid perovskite. This material has the same structure as the mineral of the same name, "perovskite," but a different chemical composition. Unlike a natural mineral with the chemical formula $CaTiO_3$, hybrid perovskites synthesized in the laboratory and used for solar cells consist of organic (methylammonium, formamidinium) and inorganic (lead, bromine, iodine ions) ions. Since such compounds combine organic and inorganic parts, they are called hybrids, and their general formula can be represented as ABX_3 (A = MA (Methylammonium), FA (Formamidinium), B = (Pb2+, Sn2+, Ge2+); X = I, Br, Cl). (Fig. 1.1.)

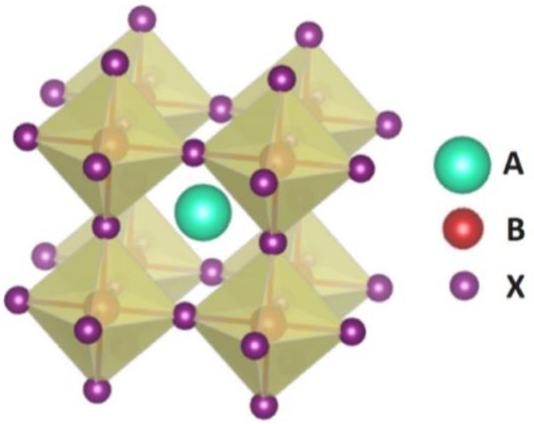

Figure 1.1. Cubic perovskite crystal structure [1]

The stability of the photoactive crystalline perovskite structure is determined by geometric criteria. It depends on the Goldschmidt tolerance factor t, which is calculated from the ratio of ionic radii A, M and X by the formula [2]:

$$t = (R_A + R_x)/\sqrt{2(R_M + R_x)}\ (1)$$

R_A, R_B and R_X are the ionic radii A, M and X. For an ideal perovskite structure, t = 1.

A perovskite or perovskite-like structure can be preserved if t takes values from ~0.8 to ~1.1. Such compounds may have a distorted crystal lattice with symmetry below cubic (tetragonal, rhombic, rhombohedral) [3]. This structure distortion seriously impacts materials' optoelectronic and magnetic properties, which can negatively affect the characteristics of devices based on photoactive perovskite systems.

The great interest of researchers in perovskite photovoltaics began in 2009 when Perovskite materials $CH_3NH_3PbI_3$ and $CH_3NH_3PbBr_3$ were first used in dye-sensitized solar cells and demonstrated light conversion efficiencies of up to 3.8% [4]. In 2012, by replacing the liquid electrolyte with solid-state materials for transferring holes, Park et al. reported a PCE of 9.7% for the first solid-state perovskite solar cell [5]. Since then, PSCs saw a rapid increase in the efficiency of the device, exceeding 25% in 2022 (Fig. 2) [6].

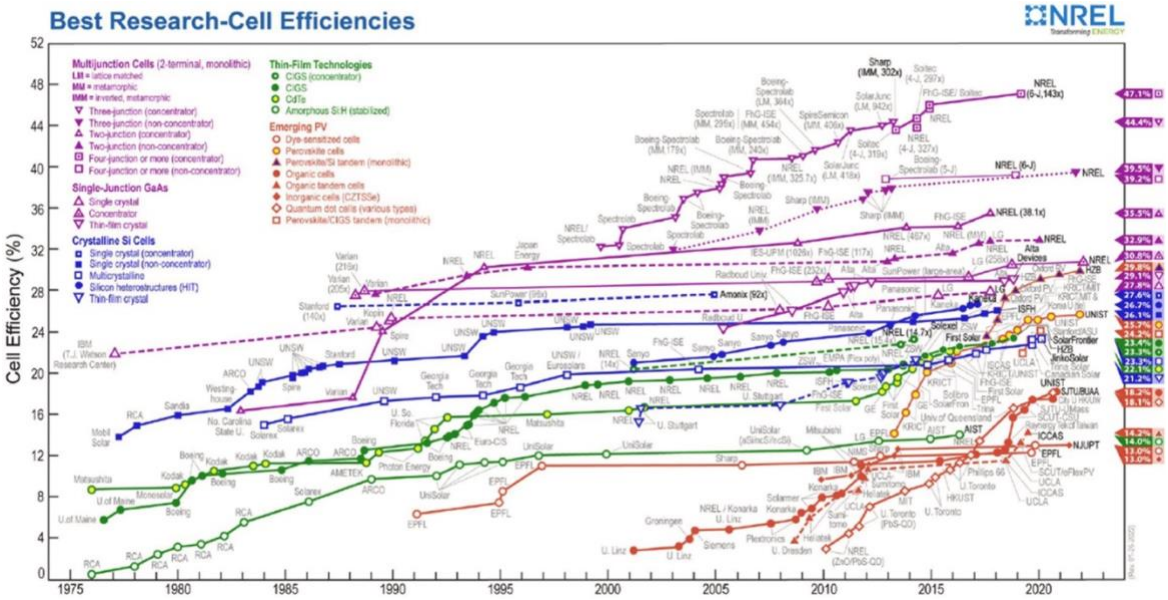

Figure 1.2. Record PCE chart, taken from the NREL, Golden, CO, USA website. [6]

1.3. Main characteristics of solar cells

A combination of three factors determines a solar cell's power conversion efficiency (PCE): The open circuit voltage (Voc) is the most significant potential produced by the device, while the short circuit current (Jsc) is the current that reaches the electrodes without any applied field. The current must be created with a particular potential to perform its intended function. An important quality indicator is the fill factor (FF), which measures how much power can be generated from the sum of Jsc and Voc. The product of three parameters is divided by input power (Pin) and indicated by sign (η).

$$\eta = \frac{P_{\text{out}}}{P_{in}} = \frac{FF(V_{oc} \times J_{sc})}{P_{in}}$$

$$FF = \frac{V_{mpp} \times I_{mpp}}{V_{oc} \times J_{sc}} \qquad \text{Equation (2) and (3)}$$

Vmpp is the voltage at the maximum power point and Jmpp is the current density at the full power point. A current density versus voltage (JV) curve representative of a solar cell is seen in Figure 3. It provides examples of the Voc, Jsc, and FF, as well as the values for the JMpp and VMpp

(JMpp and VMpp are the points on the JV curve where maximum power is produced). The underlined and shaded region may identify the FF in the graph. While the maximum power point (MPP) has the most significant yield, the voltage and the current product have the lowest yield [7].

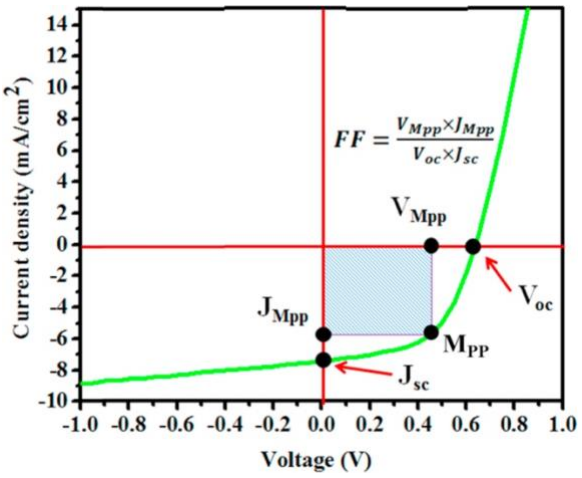

Figure 1.3. Standard Current density-voltage (J-V) curve [8].

Short circuit current density (Jsc)

The Jsc is the maximum photocurrent density generated at zero applied potential (for example, in short, circuit conditions when Voc = 0) [9]. It represents the number of charge carriers that can be generated and eventually collected at the respective electrodes when there is zero applied potential [10]. Even though no electricity is being developed at this stage, the J_{SC} signifies the beginning of power.

Open circuit voltage (Voc)

As one of the most critical elements determining the device's efficiency, Voc is a measurement of the highest voltage a solar cell can extract for use in an external circuit [11], [12]. Voc is calculated when J = 0 or open-circuited [13].

Fill factor (fill factor) (FF)

The FF is an essential quantity that influences the PCE, determined from the PCE's J-V characteristics as a product of Jsc, Voc, and FF. In addition, the shape of the J-V features is described by the FF, which is the ratio of the maximum output power to the product of Jsc and Voc [14]. This ratio describes the relationship between the highest output power and the development of Jsc and Voc. In an ideal scenario, FF should reach 100% when the J-V curve is in the shape of a rectangle [15].

Power Conversion Efficiency (PCE)

PCE is the percentage of input irradiation (Pin) that is transformed into the output power. It is the product of Voc, Jsc, and FF divided by the input power. PCE is the percentage of input irradiation (Pin) turned into the output power (Pin).

These three factors are essential when it comes to the determination and optimization of the performance of solar cells. To obtain optimal performance, every component that contributes to the device's efficiency must be improved, including the composition, interfaces, layers, electrodes, and manufacturing procedures.

1.4. Common structures of perovskite solar cells

Figure 1.4. depicts two of the most typical architectural configurations for perovskite electronic devices. PSCs with a mesoscopic nanostructure may be seen on the left, whereas planar structures can be seen on the right [16]. As was previously mentioned, structure, material, and interface modification are essential to achieve optimum device performance. In both systems, layers on each side of the perovskite layer have the potential to either stimulate or discourage electrons and holes from travelling in a specific direction to avoid charge recombination. Various materials are used in the role of electron or hole transport layers (ETL and HTL). For instance, TiO_2 is the most frequent material used for an ETL [17]; however, other metal oxides such as SnO_2 are also often utilized [18]. Regarding the HTL, organic material is often chosen since the underlying perovskite layer has temperature limits. In addition, to prevent the dissolution, a proper solvent must be selected for materials deposited on top of the formed perovskite layer. It can also be noted that

many PSCs structures include an additional passivation layer between ETL/Perovskite and Perovskite/HTL to improve interface contact, reduce carrier recombination and enhance carrier extraction to boost the overall PCE and stability of devices. [1]

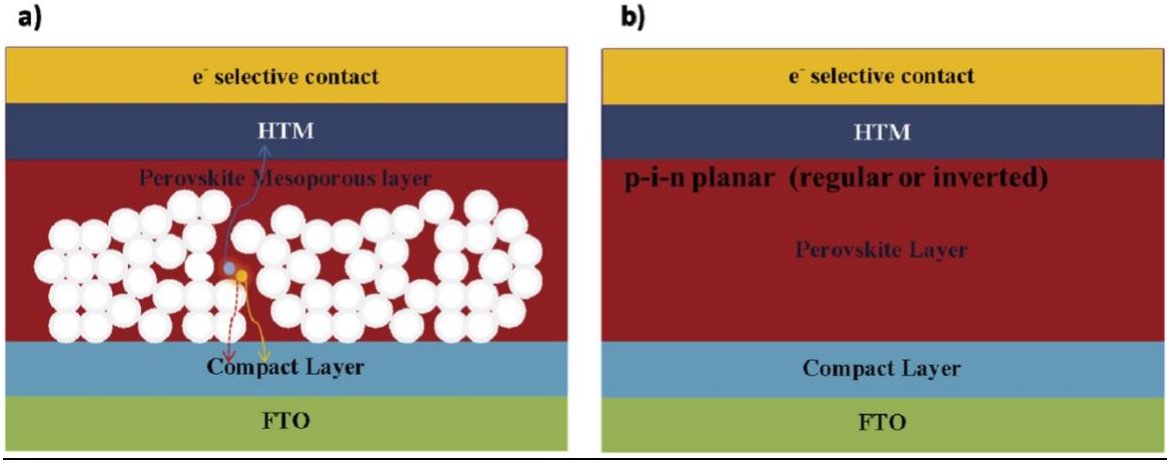

Figure 1.4. PSCs structures: Mesoscopic nano-structured (left) and Planar structured (right) [16]

1.4.1. Mesoscopic perovskite solar cells (MPSCs)

In PSCs, mesoporous (mp) materials allow the perovskite material to connect with the mp metal oxide structure. This increases the light-absorbing surface of the photoactive layer, which in turn improves the device's performance. A typical MSPSC has the following layers: a transparent conducting oxide layer (TCO) (such as FTO or ITO), an ETL layer, an mp metal oxide scaffold, a perovskite material layer, an HTL layer, and an electrode layer (Fig. 1.4) [1]. MSPSCs had already attained PCEs larger than 23% [19], which significantly improved from when Kim and his colleagues manufactured the first all-solid-state MSSC with 9% efficiency [5].

1.4.2. Planar PSCs

Although usage of low temperature (LT) (sub-150 °C) processing methods had been reported for mesoscopic PSCs via the utilization of nanoparticles [20,21], many published studies still prefer mp films, which require high-temperature (HT) processes, especially for the cells with higher PCE. Because of the insufficiency of the mp metal-oxide scaffold, planar architecture PSCs are only LT processable. This leads to a better potential for producing flexible PSCs than their mesoscopic

counterparts [1]. A planar structure provides a significant amount of flexibility in the organometal halide perovskites (OHPs) preparation, allowing various materials to be used as charge transport layer (CTL) to pair with the corresponding perovskite. For instance, compact oxides act as an electron transport layer, including ZnO, SnO_2, In_2O_3, WO_3, Fe_2O_3, and Nb_2O_5, as well as compact TiO_2 [22]. As a general rule, a high-temperature annealing step is not necessary to create thin films of compact oxides. As a result, ETLs may be simply applied with a broad range of techniques. Planar photovoltaic solar cells (PSCs) may be classified as either n-i-p (Fig. 1.5a), or p-i-n (Fig. 1.5b) types, and this categorization is based on the order of the several operational layers inside the cell, beginning with the layer upon which light is incident.

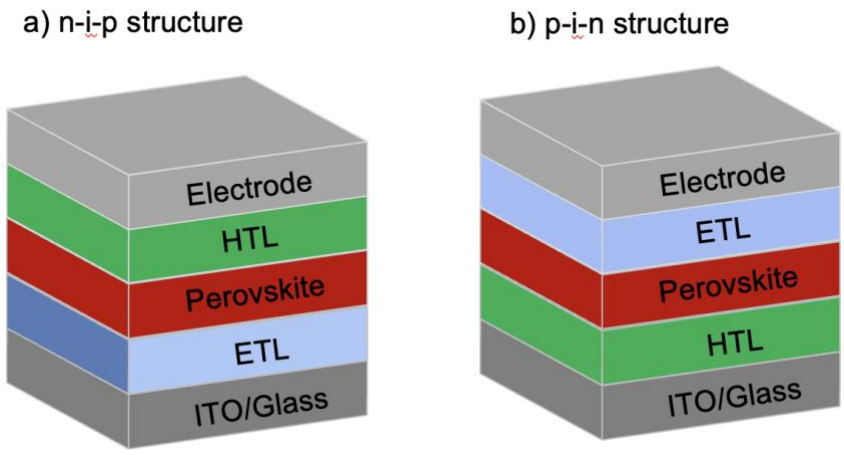

Figure 1.5. Planar n-i-p (a) and planar p-i-n (b) PSCs structures.

1.4.2.1. Planar n-i-p PSCs

In conventional n-i-p planar design, an n-type electron transport material is placed on a TCO substrate, followed by the perovskite absorber layer and p-type hole transport material, sequentially finishing with a top metal electrode on the substrate (Fig. 1.5a). The FTO/c-TiO_2/$CH_3PbI_{3-x}Cl_x$/Spiro-OMeTAD/Au structure was the first to be published with an n-i-p planar PSC structure [20]. Interfacial layers made of various charge transport materials were employed to increase charge extraction further and enhance the performance of n-i-p PSCs. Due to high hysteresis and lack of long-term stability [23], a need for the replacement of common TiO_2 and ZnO ETLs became evident. As a result, a straightforward technical procedure that utilizes

diluted SnO_2 solution as ETL processing was introduced. Shortly, devices that used tin oxide (IV) as ETL demonstrated a stable PCE of nearly 21% [24]. Still, due to poor contact interface and the recombination of charges between the corresponding CTLs and the perovskite absorber layer, efficiency and stability losses are evident in n-i-p planar PSCs [25]. For HTL, Spiro-OMeTAD was employed as an HTM in the most highly efficient PSCs. At the same time, lithium bis(trifluoromethanesulfonyl)imide (LiTFSI) and 4-tert-butylpyridine (t-BP) were used as a p-dopant in the majority of the PSCs. Because the p-type dopant has a high electron affinity, electrons from the HOMO of Spiro-OMeTAD molecules are extracted efficiently, resulting in enhanced hole density and conductivity of the HTMs [26]. On the other side, doping leads to major drawbacks like Li^+ ions migration across the cell while it is operating. This can increase the potential for perovskite redox reactions [27] and drive rapid cell degradation through moisture penetration since Li^+ salts are highly gyroscopic [28-31]. One way to improve the overall stability of PSCs is by incorporating an additional passivation interlayer between the perovskite and the HTL layer, like Lewis acid and base materials [32,33]. Overall, the n-i-p planar structure provides a range of opportunities to tackle both PSCs' efficiency and long-term stability issues.

1.4.2.2. Planar p-i-n PSCs

What makes p-i-n and n-i-p structures distinguishable is that both CTLs are inverted. The HTM is deposited on top of the TCO substrates in an inverted configuration (Fig. 1.5b). In many instances, PEDOT:PSS serves as the hole transporting layer (HTL), whereas $PC_{61}BM$ or $PC_{71}BM$ serves as the electron transporting layer (ETL). One of the main obstacles that p-i-n PSCs face is the acidic nature of PEDOT: PSS, which negatively affects cell performance and stability [34].

However, PSCs with inverted structures have some advantages over a conventional n-i-p structure because of the potential of LT preparation, the demand for dopants in the HTM, and compatibility with the organic electronic manufacturing method [35]. For the first time p-i-n structure was used with ITO/PEDOT:PSS/$MAPbI_3$/C_{60}/BCP/Al configuration and resulted in a 3.9% PCE [36]. Inverted PSCs still lag substantially behind ordinary n-i-p structured devices in terms of performance, as the highest recorded efficiency for PSCs uses conventional n-i-p structure [6, 37].

1.5 Fabrication of PSCs

Several methods, including solution processing, are available for fabricating PSCs (Fig. 1.6) [38]. It is possible to classify the solution-processed deposition of the perovskite absorbent layer into one-step and two-step methods based on the number of stages involved in the deposition process (Fig. 1.7) [39]. Because of their simplicity, reproducibility and superior photovoltaic performance, the one-step and two-step spin-coating processes have become common among PSCs researchers. Usually, a multi-component solution of precursors, solvents, additives, and antisolvents is prepared and mixed. This follows up with a spin coating process in the glove box's strictly controlled temperature and inert gas environment.

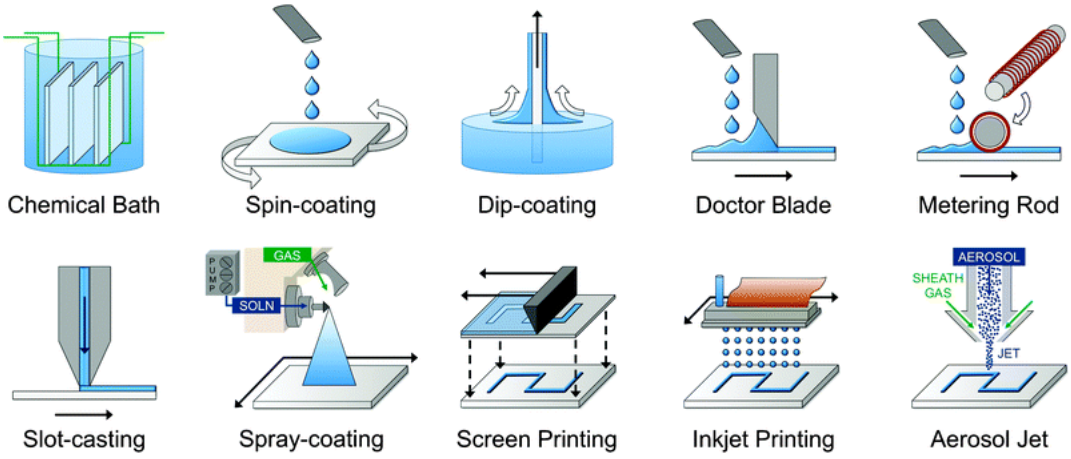

Figure 1.6. Depiction of various solution deposition methods [38].

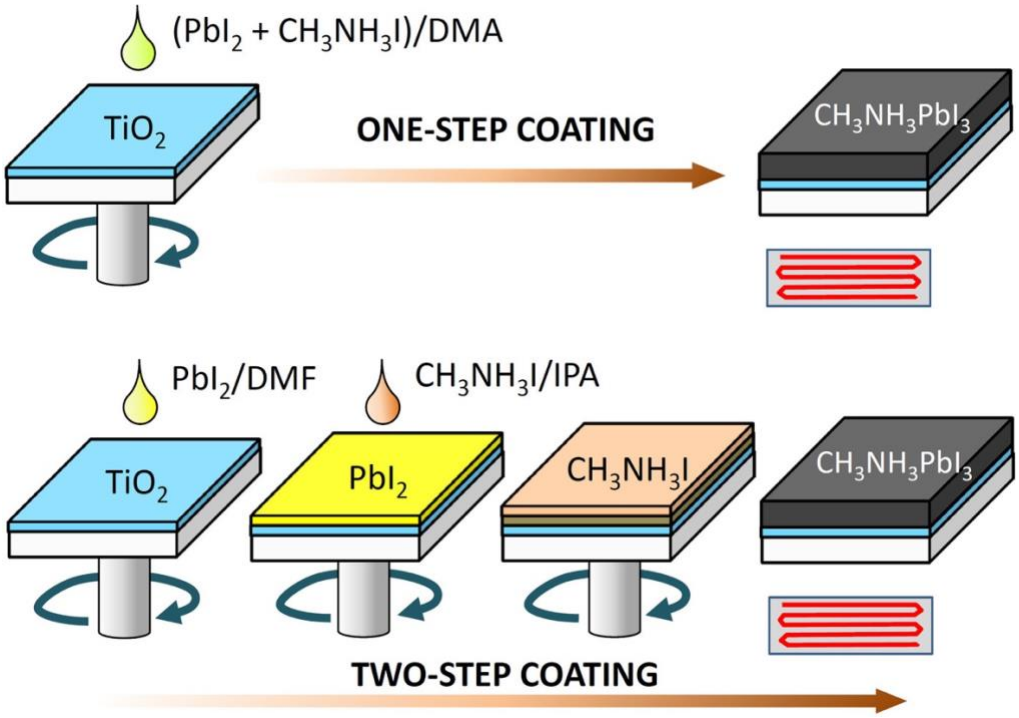

Figure 1.7. One-step and two-step spin-coating procedures for $CH_3NH_3PbI_3$ formation [39].

The one-step deposition was widely used in PSC production because of its cheap cost and simplicity. To create a perovskite film, the one-step deposition approach typically involves dissolving metal and organometallic compounds into a suitable solvent and spin-coating the mixture onto a substrate. Then, the just formed perovskite layer is annealed to the proper temperature to produce a black perovskite film.

In the two-step deposition, organic and inorganic parts of the precursor solution are split as prepared metal halide solution is spin-coated over a substrate, followed by an annealing procedure. Next, a spin-coating of an organometal halide onto metal halide films is followed by annealing to produce perovskite films. In certain situations, a metal halide layer is added to the organic salt precursor in the second phase, causing a chemical reaction that results in perovskite film.

1.6. Strategies for enhancing the efficiency of PSCs

Three strategies are used to increase the performance of PSCs.

a) Optimization of the chemical composition

Variation of the chemical composition of complex metal halides is one of the most effective ways to increase the stability of perovskite material. It has been repeatedly shown that spontaneous decomposition of $CH_3NH_3PbI_3$ into CH_3NH_3I and PbI_2 can be prevented by partially substituting iodine atoms with bromine or chlorine lead atoms with tin or germanium, organic methylammonium cation with formamidinium or cesium cations in its structure [40]. For example, $CH_3NH_3^+$ protonated $CH_3PH_3^+$, $CH_3SH_2^+$, and SH_2^+ promote the formation of strong hydrogen bonds and the substitution of I^- and Br^- more electronegative anions F^- and Cl^- increases the electronic binding between cations and perovskite octahedral cells [41]. The steric factor demonstrates high importance, too: for example, substituting a large iodide for a smaller bromide ion material leads to a decrease in the symmetry of the crystal and, consequently, to the formation of a more compact perovskite structure with improved stability [42]. However, in several studies, PSCs based on $MAPbI_{3-x}Br_x$ demonstrated low photochemical stability due to spinodal decomposition of individual phases enriched with iodine and bromine even at low temperatures around 27°C [43]. In general, the interaction between Perovskite precursor solution and its additives, especially between organic additives with multiple-functional groups, is still poorly understood despite numerous research studies that have been done so far. This necessitates trial-and-error procedures and the efficient construction of rules and protocols, which severely limits additive technology for commercial implementation [44].

b) Optimization of PSCs architecture

Alternatively, improvements in the fabrication of devices that isolate the active layer to prevent the evaporation of volatile decomposition products into the atmosphere and suppress all side reactions by using chemically inert charge-transport and electrode materials can significantly improve the operational stability of hybrid perovskite solar cells. In PSCs with a conventional

structure, the hole-transport Spiro-OMeTAD also performs the role of an insulating layer, thereby preventing the volatilization of $MAPbI_3$ degradation products. However, this is not enough to avoid the evaporation of volatile photothermal decomposition products [45,46]. In this regard, there is a need for interlayer technology, which is based on the introduction of semiconductor materials with improved insulating properties at the interface of the perovskite and the hole transport layer. To achieve firm isolation of the perovskite layer, and preserve the material balance in the system, several organic polymers and small molecules with hole-transport properties have been developed and studied [47]. At the same time, incorporating interlayer materials should not dramatically worsen the voltage characteristics of perovskite solar cells. One of these materials was poly-N-vinyl carbazole (PVK). This optimal layer thickness ensured the devices' stable operation and significantly increased the values of Jsc, Voc and FF in solar cells [48]. To safeguard the perovskite layer underneath the hydrophilic material, Ma et al. treated perovskite films on the surface using iodides such as 2-aminoethanol hydroiodide (2AEI) or 4-amino-1-butanol hydroiodide (4ABI). This led to an efficiency value of 23.25% due to lowered trap-state distribution by passivating surface defects as the hydrophilic iodides absorb water molecules on the perovskite layer [49]. However, the lengthy alkyl chains have the potential to produce a charge extraction barrier between the perovskite and the charge transport layer, which can result in inefficient charge extraction of PSCs. Therefore, determining the ideal length of the alkyl chain and the optimal values for the other chemical and physical parameters of interlayer molecules would be of considerable use for the efficient passivation of the perovskite layer. In addition, to develop novel surface-passivating molecules, it is vital to have a solid understanding of the underlying processes of surface passivation through organic salts and molecules [50].

c) Optimization of Charge Transport Layers

The light-absorbing layer is responsible for producing holes and electrons, which then make their way to the hole transport and the electron transport layers, respectively. The elimination of optical and electrical losses during this process in the device may be accomplished by optimization of ETL and HTL materials. It’s been a long and continuous work to find appropriate and optimized ETL for perovskite that would fulfil all requirements, which include complete surface coverage, high transmittance and good stability [51]. Until recently, a dense TiO_2 layer was a standard ETL

material; however, due to high-temperature annealing and lower electron mobility, it was edged out by SnO_2 with a smaller conduction band and higher charge transfer efficiency. However, SnO_2 is far from ideal ETL as comparatively low conductivity with poor wettability reduces its full potential for efficient electrons extraction from the perovskite layer [52]. Doping SnO_2 solution with additives is one of the methods that may be used to improve an ETL. Ren et al. prepared chlorinated SnO_2 (SnO_2-Cl) ETL from 1,2-dichlorobenzene and minimized the surface imperfections in the SnO_2 film, preventing the buildup of electrons; they accomplished PCE increase from 17.01% to 17.81% [53]. Liang et al. reached 20 % efficiency by synthesizing SnO_2 quantum dots (QDs) chlorinated with NH_4Cl as a solution dopant [54].

1.7 Problems with perovskite solar cells

For the production of efficient and at the same time cheap solar cells based on perovskites, these cells must have long-term operational stability. The warranty period of silicon solar cells is 20-25 years. If the efficiency of a perovskite solar battery decreases by 1% every year, then in 20 years, it will degrade by 20%, which is quite a good indicator in the field of photovoltaics [55]. Like organic solar cells, devices based on perovskite materials have significant stability problems. This is due to the perovskite material's inherent instability and external factors that have a detrimental effect on the device.

1.7.1. External factors contributing to the degradation of perovskite materials

Despite the enormous advantages of perovskite solar cells over photovoltaics, these devices are unfortunately still far from practical implementation. The main problem is the extremely low stability of complex lead halides. Halide (especially iodide) complexes of lead are rapidly destroyed at elevated temperatures and under the influence of moisture and oxygen in the air [56,57]. In addition, perovskite materials based on lead halides are characterized by low photochemical and electrochemical stability [58,59].

1.7.1.1 Hydrolysis of complex lead halides

There are instances in which humidity does not affect perovskite solar cells [60]. Perovskite films are obtained with large grain sizes and at the same time with fewer defects in the crystal structure as a result of using a controlled humidity level during the formation of the photoactive layer. Several studies reported that this contributed to a more efficient dissolution of the components of the perovskite material in the solvent [61,62]. As a result, perovskite films were obtained with large grain sizes and, simultaneously, with fewer defects in the crystal.

On the other hand, it is well known that perovskites composed of hybrid lead halides are susceptible to disintegration in the air's presence of moisture and oxygen. It has been demonstrated by several research groups that the process of hydration on the surface of $MAPbI_3$ occurs through the formation of crystal hydrates that have a composition that is not stoichiometric. This, in turn, causes the material to break down into PbI_2 and various other by-products. One of the earliest investigations of this kind was carried out by Wang et al. [63]. In their study, which was one of the first of its kind, the influence of high humidity (60%) on the chemical composition of $MAPbI_3$ films was investigated with the help of ultraviolet spectroscopy (UV) and X-ray fluorescence analysis (XFA) techniques. After 18 h of storage of $MAPbI_3$ films in air, it was discovered that, in their optical spectra, the disappearance of the absorption band of perovskite (530-800 nm) and, secondly, the appearance of the absorption band at 520 nm, characteristic of PbI_2. The results of the optical spectroscopy were confirmed by the findings of the XRD analysis, which showed that the peaks that belonged to the $CH_3NH_3PbI_3$ phase disappeared while the peaks that belonged to the lead iodide phase appeared. A plausible process for the degradation of complex $MAPbI_3$ [64] has been presented, and it is based on the data obtained. This mechanism involves numerous steps, which can be shown in Figure 1.8:

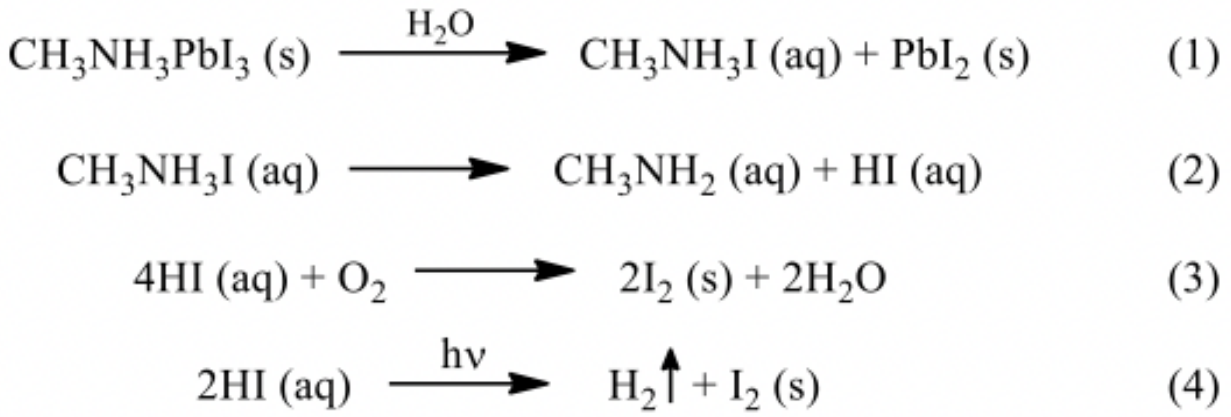

Figure 1.8. Hydrolysis of Perovskite compound with H_2O [64]

It is assumed that in the first stage, $CH_3NH_3PbI_3$ undergoes hydrolysis to form PbI_2 and a solution of CH_3NH_3I (reaction 1). Then CH_3NH_3I decomposes into CH_3NH_2 and HI (reaction 2). Then, under the action of oxygen in the air (reaction 3) and light (reaction 4), HI decays into I_2 and H_2 [64].

Other authors have proposed different mechanisms of degradation of complex lead halides under the influence of moisture. Kelly et al. investigated the degradation processes of the material using the sliding incident X-ray method (GIXRD) [65]. They found that at 80% humidity, the decomposition of $MAPbI_3$ occurs through the formation of a hydrated intermediate $(CH_3NH_3)_4PbI_6 \cdot 2H_2O$ containing an isolated octahedron PbI_6^{4-}.

1.7.1.2. The effect of air oxygen on the stability of complex lead halides

In 2015, a paper was published showing how $MAPbI_3$ films undergo photochemical degradation even in a dry air atmosphere, which indicates the reaction of iodides with oxygen. Using a set of complementary methods, such as nuclear magnetic resonance (NMR), X-ray diffraction and Raman spectroscopy, it was found that sunlight irradiation of films of perovskite material in a stream of dry air leads to the formation of methylamine, lead iodide, molecular iodine and water molecules [66]. The mechanism of this process is shown in Figure 1.9, from which it can be seen that photoexcited electrons of $CH_3NH_3PbI_3$, reacting with molecular oxygen, form superoxide (O^{2-}

). Then O^{2-}, interacting with $CH_3NH_3PbI_3$, deprotonates the methylammonium cation, ultimately forming the above reaction products.

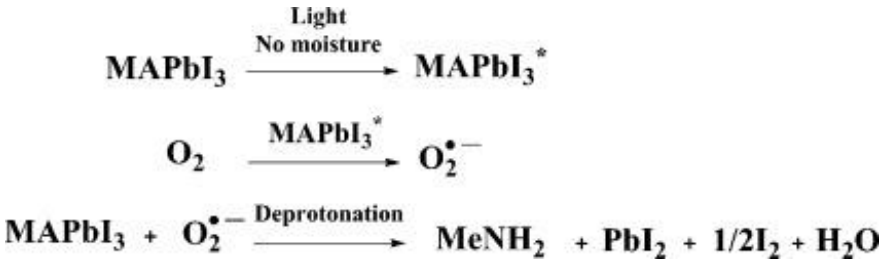

Figure 1.9. Reaction scheme for the possible perovskite degradation with oxygen [66]

A similar study [67] in which films and devices based on $CH_3NH_3PbI_3$ were put through degradation tests for a period of 48 h under a variety of conditions (A – white light and nitrogen atmosphere, B – darkness and dry air, C – white light and dry air, D – white light and humidity), discovered that factors C and D were the most damaging to $MAPbI_3$ films. Therefore, oxygen negatively influences perovskite materials, particularly $MAPbI_3$, whether it is present in the presence of light or not. This is true whether the oxygen is present in the dark or in the fact of light. This suggests that oxygen will not only have a detrimental effect on the stability of PSCs but also on the operational features of devices that can work when it is dark (transistors, sensors, etc.).

Figure 1.8 demonstrates that when perovskite films are exposed to oxygen, the process of perovskite film disintegration starts at the interface and subsequently spreads to the grains themselves [68]. In addition, this process's progression may occur even when there is little oxygen present in the atmosphere—no more than 1%.

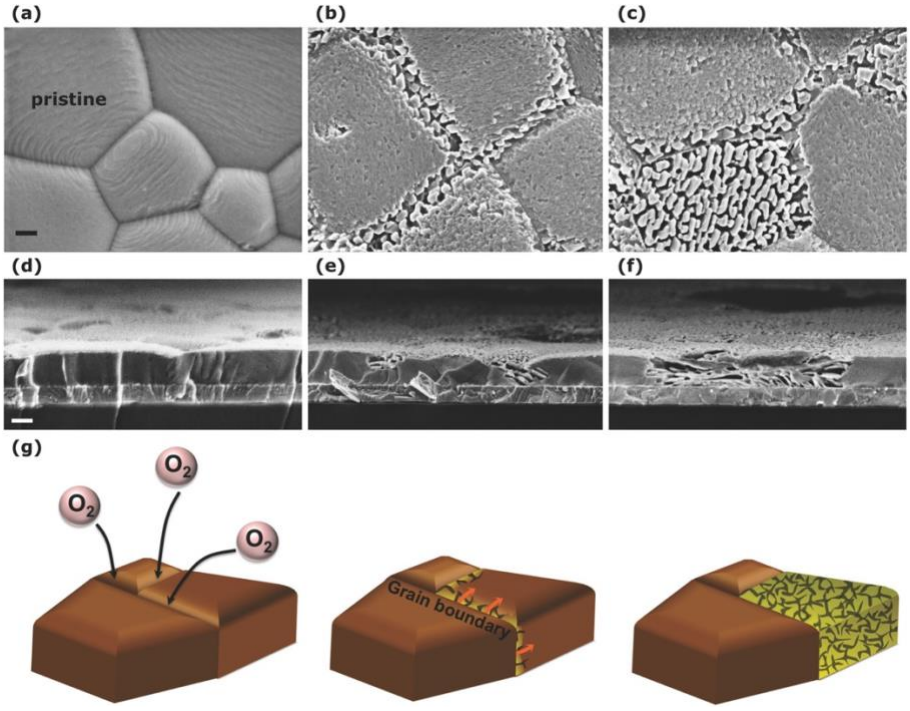

Figure 1.10. SEM top view and cross-section pictures of $PbAc_2$ on ITO: a,d - pristine layers, b,e - initial stages of degradation, and c,f - later stages of degradation, g) progression of oxygen-induced degradation from the grain boundaries [68].

Therefore, the high chemical reactivity of complex lead iodide may be inferred from the poor stability of perovskite materials about H_2O and O_2 reactions. Because the photoactive layer will be in continuous contact with solvents, dopants, components of buffer layers, and electrodes, this facet must be taken into consideration during the production of PSCs.

1.7.2. Internal factors limiting the stability of perovskite solar cells

An electric field, high temperatures, and light all contribute to a breakdown of the active layer components of a solar cell's active layer. Encapsulation or other technical methods cannot stop the degradation processes referred to above, which are entirely internal—for this reason, verifying that the films made from these materials are indeed stable under real-life working circumstances of

solar cells before contemplating the commercialization and widespread practical application of perovskite photovoltaics is vital.

1.7.2.1. Electrochemical degradation and the primary decomposition products of perovskite materials

One of the primary causes for the formation of hysteresis in the voltage characteristics of perovskite devices is the movement of ions ($CH_3NH_3^+$, Pb^{2+}, I^-) in an electric field. Because metal ions may migrate into the photoactive layer under the influence of flowing current, anions of complex lead halogens migrate to the anode, causing a deforming voltage. This process is particularly undesired [67]. The vacancy concentration at the anode is lower than the overall volume of perovskite material, according to the Nabarro-Herring creep hypothesis. As a result, the PSCs are degrading quickly as there is an increased risk of material damage in interface regions because of the disparity in hole concentration.

A large number of studies have examined the energy of defect generation in the interaction between crystal defects (MA_I, Pb_I, I_{MA}, and I_{Pb}) and interstitial atoms (MA_i, Pb_i, and I_i), as well as vacancies and interstitial cations (MA_{Pb} and Pb_{MA}) (V_{MA}, V_{Pb} and V_I). As their formation energy is low, crystalline defects that are both kinetically and energetically unstable may be quickly disintegrated into their corresponding vacancies and interstitial atoms. Angelis et al. [68] computed alternative migration pathways for vacancies and defects along the perovskite crystal and demonstrated four simulated systems shown in Figure 1.9. Dotted circles correspond to vacancies in this figure, and red atoms correspond to interstitial defects. Dotted arrows show the trajectory of vacancies, while solid lines show the migration of ions [68].

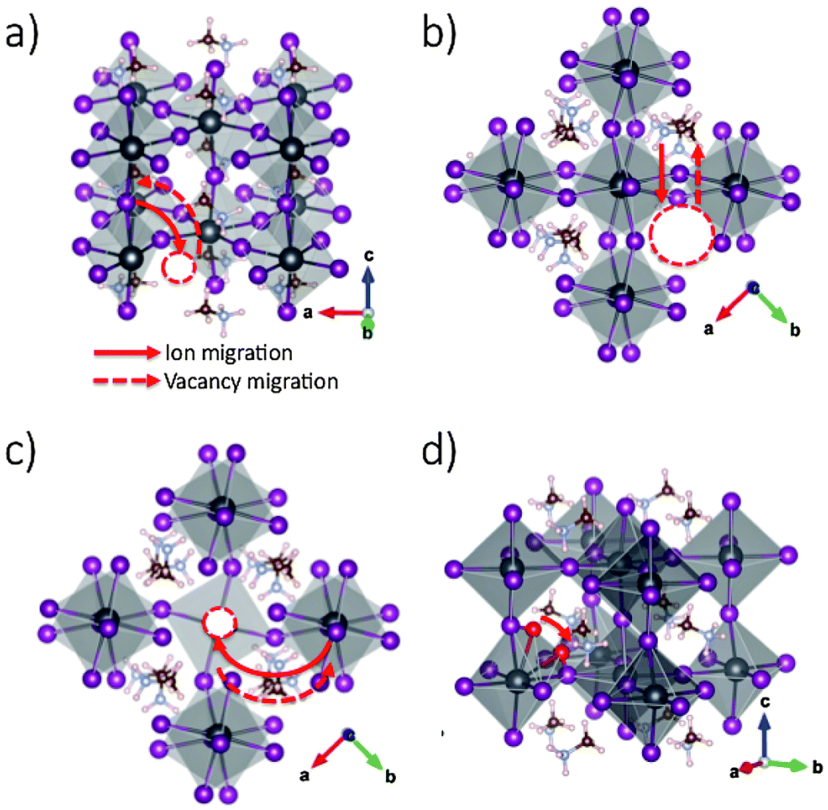

Figure 1.11. Diffusion paths for the V_I (a), V_{MA}, (b), V_{Pb} (c) and I_i defects (d). For I_i, the initial and the final configurations are shown. Vacancies are highlighted with dashed circles. Red atoms refer to interstitial defects. Solid lines stand for the migration of the ions, whereas dashed lines indicate the trajectory of the vacancy. White = H, brown = C, blue = N, purple = I, and black = Pb atoms [68].

1.7.3. Hysteresis

The hysteresis index (HI) is a metric that used to determine hysteresis severity

$$HI = (PCE_{RS} - PCE_{FS})/PCE_{RS}$$

where PCE_{RS} and PCE_{FS} are the power conversion efficiencies for the reverse scan (RS) with biased voltage from VOC to 0 V and forward scan (FS) with biased voltage from 0 V to Voc, respectively [69]. Hysteretic behaviour is characterized as a delay between the change in the parameters of the system caused by an external stimulus, such as an electrical or optical field. This phenomenon has been widely recorded in PSCs and hinders the potential implementation of PSCs

in the commercial sphere. It has been proposed that the origins of this phenomenon include the trapping and releasing of charge carriers at deep trap sites created by defects, the ferroelectric polarisation of perovskites, capacitive effects, and ion migration associated with a shift in the interfacial field and barriers caused by the accumulation of ions at interfaces [69]. Hysteresis was proven to be affected by the standards used for measurement. According to Unger et al., the J–V measurement scan direction, delay period, pre-measurement lighting, and voltage bias limitations significantly impact hysteresis and PCE. Significant hysteresis was reported for mesoporous and planar devices with a short decay period of 10 ms. Because the devices' reaction times are slow, there is minimal hysteresis at either high or low scan speeds (Fig. 1.10).

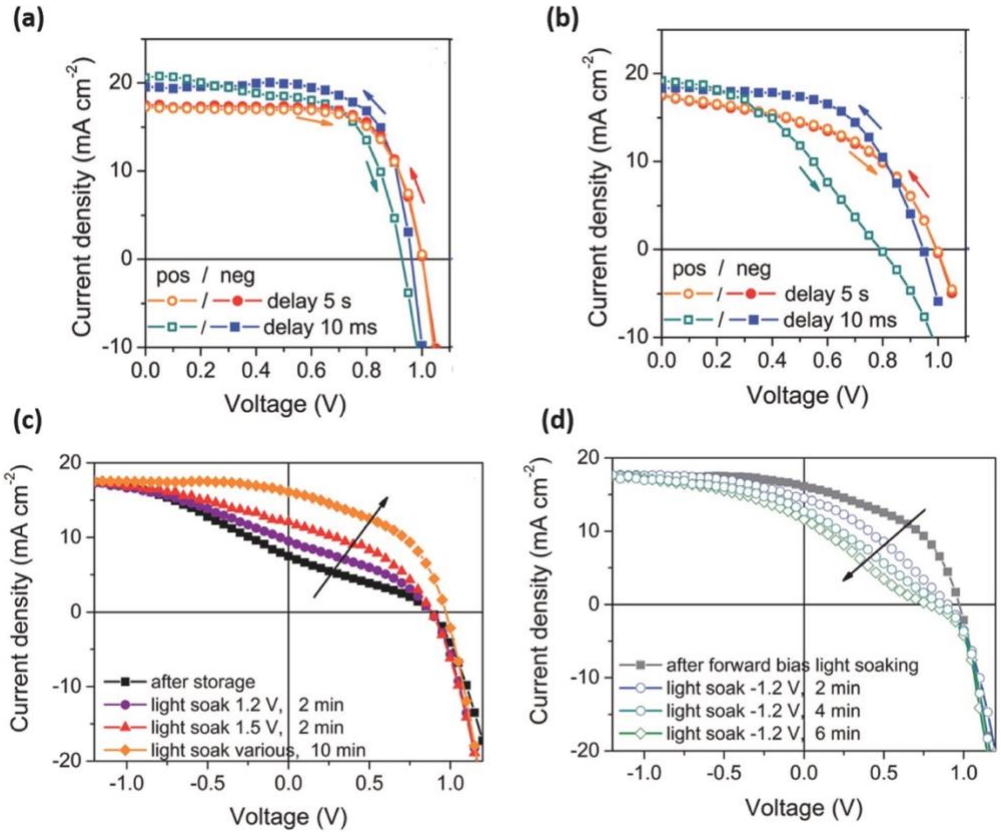

Figure 1.12. J-V measurements of (a) mesoporous and (b) planar PSCs in different scan directions (positive: 0 V to forward bias, negative: forward bias to 0 V) and delay times (0.01 s for a fast scan and 5 s for a slow scan); J-V measurements of (a) mesoporous and (b) planar PSCs in different scan directions (positive: 0 V to forward bias, negative: forward bias to 0 A light is soaking at position (c) forward bias and position (d) reverse bias [69].

1.8. Goals and objectives

It can be concluded from the literature review that the development of hybrid complex lead halides with a perovskite structure is the most promising research direction in the field of a new generation of renewable energy. However, it is essential to continue comprehensive research of PSCs, especially in stability and efficiency improvement, to ensure this technology can soon step into the commercial market.

There are a number of significant drawbacks associated with hybrid perovskites, including their low resistance to a variety of external agitators such as oxygen and moisture which results in relatively low efficiency and reproducibility of PSCs. In this regard, researchers are tasked with finding ways to prevent the degradation of perovskite materials, simultaneously improving PCE. Various approaches have been proposed to stabilize devices based on complex lead halides, from optimizing the chemical composition of perovskite films to architectural optimization. However, to find appropriate solutions to the issues above, a deeper understanding of the processes, especially the interaction between charge transport and perovskite layers, is necessary.

The primary purpose of this thesis work is to improve the operational efficiency, stability and reproducibility of perovskite solar cells based on holistic, cheap and straightforward compositional and interface stabilization of perovskite and charge transporting layers. To achieve this goal, the following tasks were solved:

1. Development of a stable, reproducible way of PSCs fabrication as a control device.
2. Development of new methods PSCs modification that can tackle current efficiency and stability issues that PSCs face without convoluted fabrication alterations and high cost.
3. Systematic study and evaluation of optical, morphological and performative characterizations using various analytical techniques and equipment, including AFM, SEM, UV-vis and Solar simulator.
4. Conducting a comparative study of the efficiency and stability of control and modified PSCs and identification of correlations between the compositional change and improved parameters.
5. Evaluation of the prospects of the studied systems and their future implications.

As a result, it was established that SnO_2-based ETL, through forming a complex with an amino polycarboxylic chelating agent named EGTA, can improve surficial properties, reduce defects and increase the efficiency of the control device by nearly 15%. Secondly, by passivating the perovskite surface defects at the perovskite/HTL interface with the dicyanobenzene isomers, the efficiency of PSCs jumped from 18.12 to 21.07 % while stability improved for additional hundreds of h. This way, it can be concluded that the quality of PSCs can be significantly enhanced through simple yet effective compositional and architectural modifications of both perovskite and charge transport layers without cost and fabrication sacrifices.

CHAPTER 2

EGTA-SnO_2 complex as an effective electron transport layer for perovskite solar cells

ABSTRACT

The electron transport layer (ETL) serves an essential role in perovskite solar cells leading to better charge extraction and stabilization of the whole device structure. Herein, we introduced ethylene glycol-bis(2-aminoethylether)-*N,N,N′,N′*-tetraacetic acid (EGTA), an organic metal complex reagent, to SnO_2-based ETL to stabilize SnO_2 colloids and enhance the surficial properties of the film. As a result, EGTA-SnO_2-based ETL film possesses better wettability and higher smoothness which facilitates high-quality perovskite grain growth. With higher conductivity and lower trap density, EGTA-SnO_2-based perovskite devices' efficiency jumped from 18.63% to 21.14%, with negligible hysteresis. In addition, unencapsulated EGTA-SnO_2-based PSCs demonstrated higher stability, retaining over 80% of efficiency in 500 h in an ambient environment and 90% in a 1000 h period in an inert atmosphere.

2.1 INTRODUCTION

Metal-organic hybrid perovskite material has gained interest in the academic sphere due to its unique semiconductor properties – long travel lengths of charge carriers, low rates of surface recombination, high mobility of electrons and holes for microcrystalline material and strong optical absorption in the visible range of the solar spectrum [70-74]. The efficiency of PSCs has increased to over 25% in a decade [6]. In standard device structure (indium tin oxide (ITO))/electron transport layer (ETL)/perovskite absorber/hole transport layer (HTL)/metal anode, all layers are chosen specifically to facilitate high efficiency and long-term stability of the overall device. In this case, ETL plays an essential role in extracting generated electrons while simultaneously blocking holes to inhibit electron-hole recombination on the perovskite surface [75]. One of the widely applicable materials for ETLs is the mesoporous TiO_2 structure due to its excellent photoelectric properties [17]. However, relatively high hysteresis levels [76] and high-temperature processing (>500 °C) [77] were needed for the formation of TiO_2-based ETL hindered cell performance and complicated the overall fabrication of PSCs. In addition, sensible to the UV part of the spectra, TiO_2-based PSCs lack long-term stability due to severe photodegradation [76]. Among other n-type

metal oxides, SnO_2 took a significant track to be the most suitable ETL for PSCs [18]. This is due to its appropriate band alignment with perovskite structure, high transmission, carrier mobility and significantly lower fabrication temperature (less than 100 C) [78]. Currently, the highest efficiency recorded up to date for PSCs is based on SnO_2 as ETL [6]. Despite significant improvements, the efficiency of PSCs is still far from the Shockley-Queisser limit, which is 33.7% [79]. In addition, the basicity of SnO_2 often leads to poor film quality that limits the application of SnO_2 as ETL [80]. To combat these issues, several techniques are incorporated into fabrication methods of SnO_2-based ETL like chemical doping and surface modification to improve SnO_2 film [81]. The standard fabrication method for SnO_2 ETL is based on diluting commercially available SnO_2 aqueous nanoparticle solution to a needed concentration and further coating a small amount of solution on the ITO surface. Due to attractive van der Waals interactions in inorganic colloid solutions, SnO_2 nanoparticles are unstable and form large agglomerates [82]. To tackle this issue, You et al. incorporated an HP (heparin potassium) polymer into SnO_2 colloid solution to regulate the arrangement of SnO_2 nanocrystals, which produced devices with 23.03% efficiency with suppressed hysteresis, high open-circuit voltage and increased electron mobility [82]. One of the other issues that SnO_2 ETL faces are unstable morphology. The interface between the SnO_2 ETL and the perovskite layer formed under low-temperature conditions produces a high number of defects that result in charge trapping and penetration of oxygen and moisture [82-84]. Various molecules with different functional groups were implemented to improve the surface properties of the SnO_2 layer and contact with the perovskite layer. For instance, Yoo et al. improved film coverage, thickness and composition of SnO_2 through a chemical bath reaction of urea, TGA (thioglycolic acid), $SnCl_2 \cdot 2H_2O$ and reached a record 25.2% performance [85].

In this work, EGTA was introduced into the SnO_2 colloidal solution. Through forming a complex with SnO_2, EGTA-SnO_2-based ETL devices reached an efficiency of 21.14% with high reproducibility at low-temperature fabrication conditions. Furthermore, EGTA-treated SnO_2 solution showed better surface coverage and improved electron mobility compared to untreated SnO_2-based ETL while simultaneously reducing the number of defects on the interface between ETL and perovskite layers resulting in negligible hysteresis of devices. Unencapsulated EGTA-SnO_2-based PSCs also demonstrated higher stability at ambient conditions retaining over 80% of initial efficiency over 500 h.

2.2 RESULTS AND DISCUSSION

Due to its long, flexible chain and numerous oxygen donors, EGTA offers several sites for the chelation of metal ions, which, in the presence of an appropriate co-ligand, results in the formation of a coordination ligand [86-89]. To enhance the electrochemical characteristics of standard SnO_2 ETL, the EGTA-Tin oxide (IV) (EGTA-SnO_2) complex has been produced. The complex formation that took place when SnO_2 reacted with EGTA aqueous solution, which resulted in the creation of a chelate, is shown in Figure 2.1.

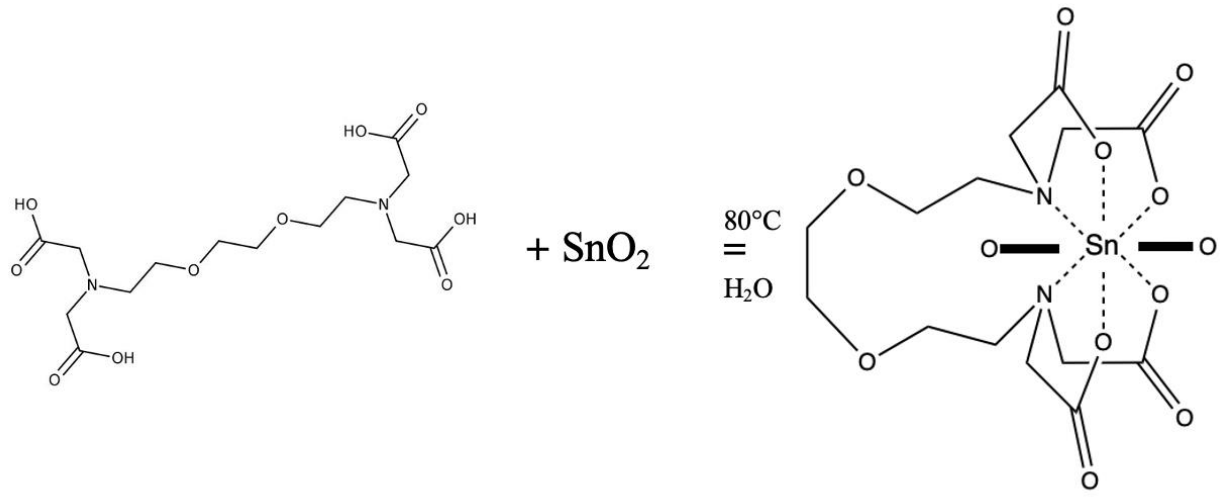

Figure 2.1. The chemical reaction of EGTA and SnO_2 at 80 °C. (Hydrogen atoms are omitted for better visualization.)

To examine the stability of EGTA complexed SnO_2 (EGTA-SnO_2) solution, samples of EGTA, SnO_2, and EGTA-SnO_2 solutions were left for an extended period. After two months, the EGTA-SnO_2 solution showed no visible change compared to the original solution, demonstrating its high stability (Figure 2.1 (a) and (b)). The FTIR spectra of EGTA, SnO_2, and EGTA-SnO_2 solution are shown in Figure 2.1c for comparison. FTIR was utilized to investigate the interaction between SnO_2 and EGTA. As can be seen in Figure 2.1 (c), the peaks in the region at 1450 and 1673 cm^{-1} correspond to the C–H bending and the C=O stretching vibrations in the EGTA. The distinctive peak at 701 cm^{-1} is due to the stretching of Sn–O in SnO_2. In addition, the peak at 1000 cm^{-1} for the SnO_2 film is attributable to the O–O stretching vibrations, which are caused by oxygen

adsorption on the SnO_2 surface [90]. In the case of the EGTA-SnO_2 sample, the characteristic peaks belonging to SnO_2 shifted and weakened compared to the pure SnO_2 sample, indicating that EGTA formed a complex with SnO_2. Atomic force microscopy (AFM) images of SnO_2 and EGTA-SnO_2 films deposited on ITO substrates are shown in Figures 2.1 (d) and (e) to analyze the morphology of newly generated ETLs. The root-mean-square (RMS) roughness of the EGTA-SnO_2 film is 2.23 nm, which is smaller than that (3.02 nm) of the SnO_2 film. This is a critical characteristic for ETL in the PSCs [91] because a smoother ETL is beneficial for the growth of the subsequent perovskite layer. In addition, we investigated the impact of EGTA modification on the wettability of the SnO_2 films by measuring the contact angles of the films (Figure 2.1 (f) and (g)). The average contact angle of the SnO_2 film was 8.47 degrees, while the EGTA-SnO_2 film had a much lower contact angle of 5.86 degrees demonstrating higher wettability of the EGTA-SnO_2 layer. The decreased roughness and improved wettability are expected to have favourable impacts on the growth of a high-quality perovskite layer [84]. The conductivity of ETLs can be measured by utilizing structures of ITO/SnO_2 or EGTA-SnO_2)/Ag, measuring IV curved and calculated using equation 4 [92]:

$$\sigma = ID(AV)^{-1} \qquad (4)$$

where A is the area of samples and D is the thickness of the ETL layer. From Figure 2.1 (h), the conductivity of the SnO_2 ETL was calculated to be 2.4×10^{-6} S cm^{-1}. Under similar circumstances, the conductivity of the EGTA-SnO_2 ETL revealed a higher value at 4.29×10^{-6} S cm^{-1}. Improved conductivity implies that the contact resistance is minimized, which can lead to higher FF and Jsc of PSCs.

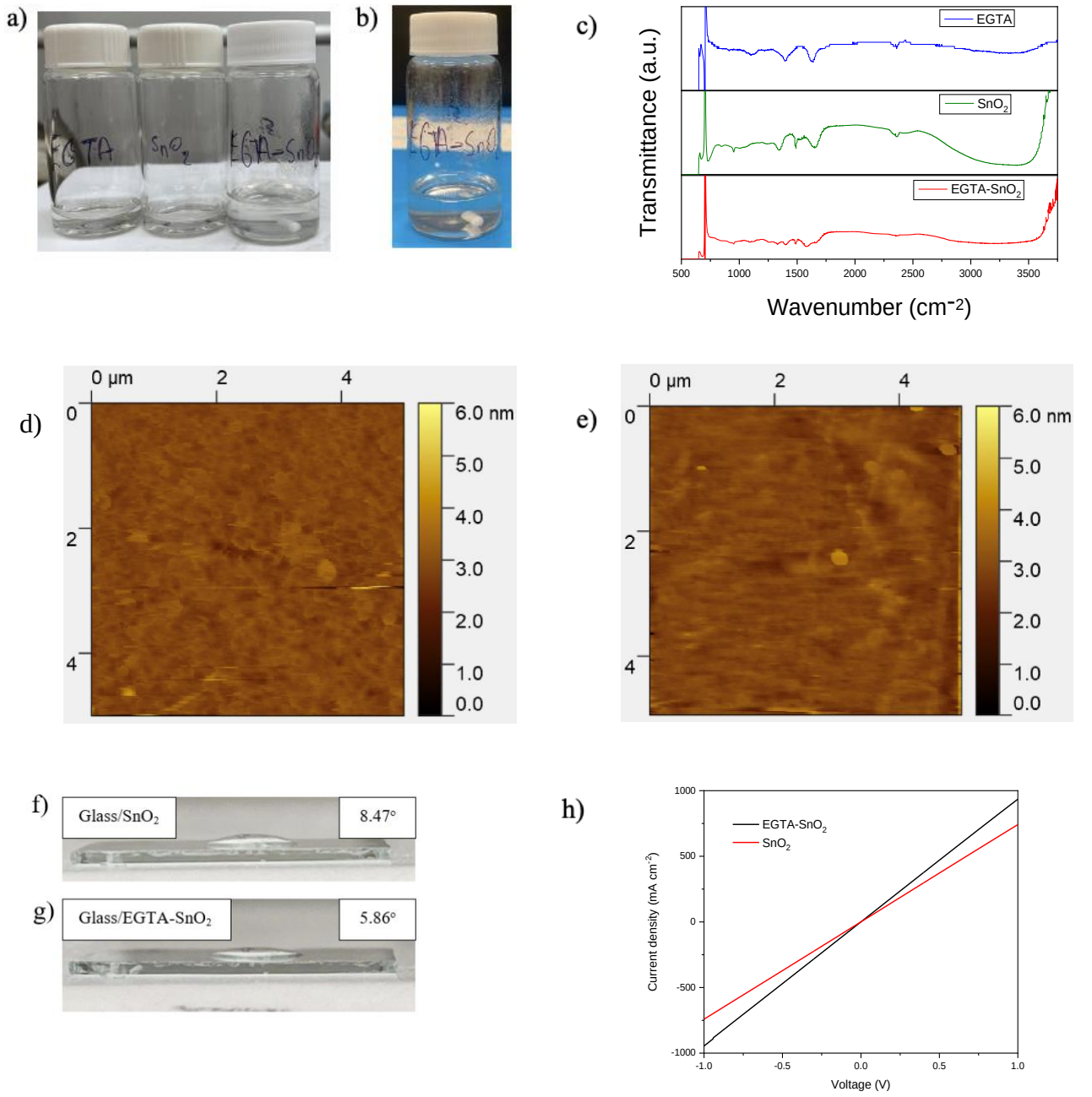

Figure 2.2. a) EGTA, SnO_2 and EGTA-SnO_2 solution right after preparation; b) EGTA-SnO_2 solution after 2 months; c) FTIR spectra of EGTA, SnO_2 and EGTA-SnO_2; d-e) AFM pictures of ITO/ SnO_2 and ITO/EGTA-SnO_2 surface; f-g) Contact angles of Glass SnO_2 and EGTA-SnO_2 films; h) J− V characteristics of the device ITO/SnO_2 and ITO/EGTA-SnO_2/Ag under dark

2.2.1. Influence on perovskite film

Perovskite ($MA_{0.9}FA_{0.1}PbI_3$) layer was spin-coated onto SnO_2 and EGTA-SnO_2 ETLs. It can be seen that the grain size (average 423 nm on average) of the perovskite layer (Figure 2.1 (a)) grown on the SnO_2 film is much smaller than that (average 828 nm) of the perovskite layer grown on the EGTA-SnO_2 film (Figure 2.1 (b)). In addition, the grain boundaries of the perovskite layer grown on the EGTA-SnO_2 film also decreased, resulting in a more compact film that can improve carrier transport and suppress carrier recombination. According to the AFM results, the EGTA-SnO_2-based perovskite layer had a smoother surface than the SnO_2-based perovskite layer, with a reduction in surface roughness from 15.2 nm to 9.2 nm (Fig. 2.1 (c) and (d)). Absorption spectra of the perovskite layer grown on EGTA-SnO_2 showed a slightly higher absorbance compared to regular SnO_2 treated substrate (Figure 2.1 (e)). Perovskite (110), (220) and (310) crystal planes are formed by the XRD pattern's characteristic peak at around 13.9, 28.0, and 31.5, respectively [93]. The enhanced intensity of the XRD patterns at 14.1° confirms the greater crystallinity of EGTA-SnO_2 perovskites, indicating that EGTA-SnO_2 is favourable to the formation of perovskite films (Figure 2.1 (f)). For a high-quality perovskite film, the low surface energy can be provided by the smaller contact angle from the EGTA-SnO_2 layer (Fig. 2.2 (g)) [94]. Additionally, the intensity of the peak at 12.7° of the EGTA-SnO_2-based perovskite film, which originated from the unreacted PbI_2, is weaker compared to the SnO_2-based perovskite film, indicating the existence of a smaller amount of this impurity in the former. Since PbI_2 tends to exist at the grain boundaries, the observed decrease in grain boundaries in the EGTA-SnO_2-based perovskite film (Figure 2.2 (b)) can be closely related to the reduction in the amount of PbI_2 [95,96]. The small increase in UV-vis absorption for the EGTA-SnO_2-based perovskite layer may also be due to the presence of fewer grain boundaries and/or fewer PbI_2 impurities [97].

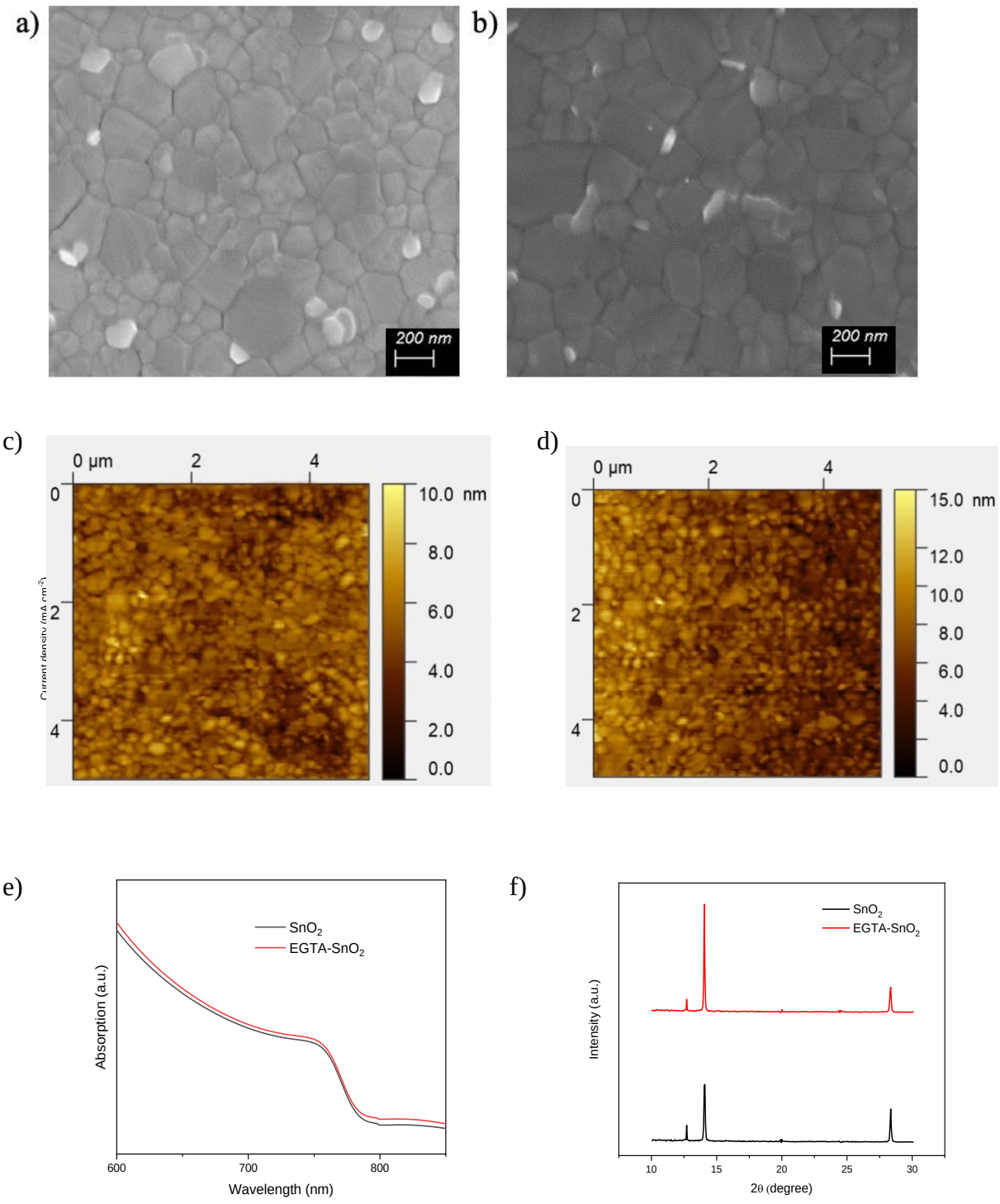

Figure 2.3. a) and b) SEM pictures of SnO_2 and EGTA-SnO_2-based perovskite films; c) and d) AFM pictures of SnO_2 and EGTA-SnO_2-based perovskite films; e) UV-Vis absorption spectra for SnO_2 and EGTA-SnO_2-based perovskite films; f) XRD spectra for SnO_2 and EGTA-SnO_2-based perovskite films.

2.2.2. Charge transfer dynamics

To evaluate the trap density of the perovskite formed on different ETL, the electron-only devices with ITO/ETL (SnO_2 and EGTA-SnO_2)/perovskite/PCBM/Ag structure were fabricated. The current-voltage (I-V) curves of the devices in dark light are shown in Figures 2.3 (a) and (b). The linear correlation corresponds to an ohmic response at low bias voltage. The current nonlinearly rises (orange line) when the bias voltage is above the kink point, which is defined as the trap-filled limit voltage (V_{TFL}), indicating that the traps are filled [98].

Equation (5) can be used for calculating the trap density (N_t) [98]:

$$N_t = \frac{2\varepsilon_0 \varepsilon V_{TFL}}{eL^2} \quad (5)$$

where ε_0 is the vacuum permittivity (8.854×10^{-12} $CV^{-1}m^{-1}$), ε is the relative permittivity or dielectric constant of the perovskite, e is the elementary charge (1.602×10^{-19} C), and L is the thickness of the perovskite film.

Using Equation (5), the trap density of the SnO_2-based perovskite layer was calculated to be 3.24×10^{16} cm^{-3}, which is twice that of the EGTA-SnO_2-based perovskite layer (1.56×10^{16} cm^{-3}). The results clearly show that the EGTA-SnO_2 ETL has the ability to improve the quality of the perovskite film while simultaneously reducing interface flaws between the perovskite and ETL as shown by a decrease in the trap density. The incident photon-to-charge conversion efficiency (IPCE) spectra and their related integrated current density are shown in Fig. 2.3 (c), which compares PSCs based on SnO_2 and EGTA-SnO_2 ETLs. It can be seen that SnO_2 and EGTA-SnO2-based devices provide integrated current values of 20.58 and 23.15 mA cm^2, respectively, which agree well with the measured Jsc values (20.66 and 23.78 mA cm^2, respectively) of the same PSCs (Table 1). When compared to the SnO_2-based device, the EGTA-treated device has a higher IPCE in the absorption region between 300 and 750 nm, which results in improved photon current. Figure 2.3 (d) shows the steady state photoluminescence (PL) spectra of the perovskite layers deposited on the top of ITO, SnO_2/ITO and EGTA-SnO_2/ITO substrates. When compared to the perovskite/SnO_2/ITO and perovskite/ITO samples, the PL quenching of the perovskite/EGTA-SnO_2/ITO sample is much more efficient. This may be related to the previously described improvement in conductivity of EGTA-SnO_2 ETL in comparison to the SnO_2 ETL.

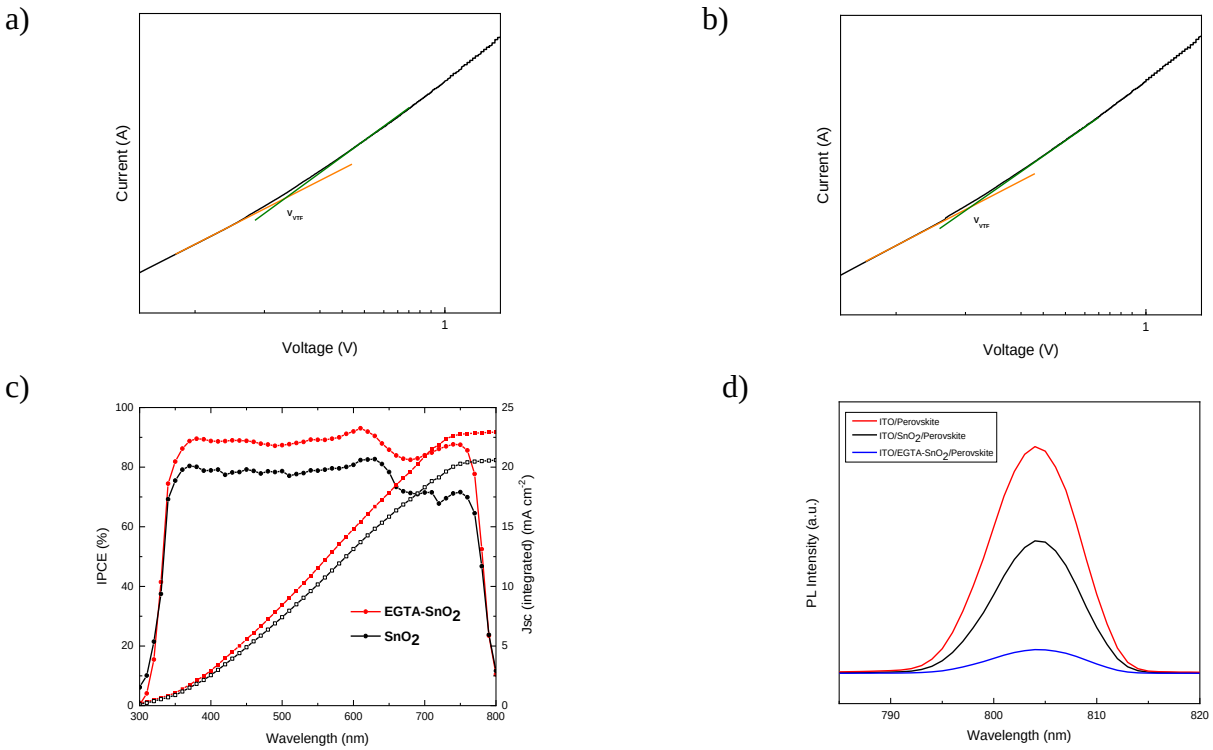

Figure 2.4. (a) and (b) SnO_2 and EGTA-SnO_2 dark I–V curves of the electron-only devices with the V_{TFL} kink points; (c) SnO_2 and EGTA-SnO_2 IPCE and the integrated current density from curves; (d) PL spectra of ITO/perovskite, ITO/SnO_2/perovskite; ITO/EGTA-SnO_2/perovskite.

2.2.3. The performance and stability of PSCs

Fig. 2.4 (a) and (b) show the J-V curves of the top-performing PSCs in backward and forward scan directions for SnO_2 ETL and EGTA-SnO_2 ETL-based PSCs. For the devices based on EGTA-SnO_2, the J–V curve virtually stays the same, indicating that hysteresis is insignificant, while for the SnO_2 ETL-based device hysteresis is close to 0.1. Interfacial capacitance induced by charge buildup at the interface, which results from ion migration, high trap density, and imbalanced charge transport in the perovskite device is often attributed to the hysteresis of PSCs [24, 99]. The higher quality of the perovskite film and improved interfaces can be accounted for small hysteresis of the EGTA-SnO_2 ETL-based PSC.

Table 1 and Fig. 2.4 (c) and (d) show statistical numbers for Jsc, Voc, FF and PCE of 30 devices. The highest efficiency of 21.14% for the EGTA-SnO_2 ETL-based device was obtained at an EGTA concentration of 0.26 mg/ml, which has improved significantly compared to the control SnO_2 ETL-

based device, which has the best efficiency of 18.63%. For practical applications, device stability is a critical metric for evaluating a solar cell. Device stability in ambient and glovebox settings was tested and compared in Fig. 2,4 (e) and (f) to highlight the impact of the EGTA-SnO_2 ETL. When kept in an N_2-filled glove box for over a month, the device based on the EGTA-SnO_2 ETL retained >80% of its original PCE. After 500 h of storage in the dark under ambient conditions (22 °C and 30-40% relative humidity) without encapsulation, the SnO_2 ETL-based device retained less than 80% of its original efficiency, while the EGTA-SnO_2 ETL-based device still had ~90% of its initial efficiency. The low trap density and fewer degradation centers brought about by the improved perovskite quality are responsible for reducing device degradation.

a)

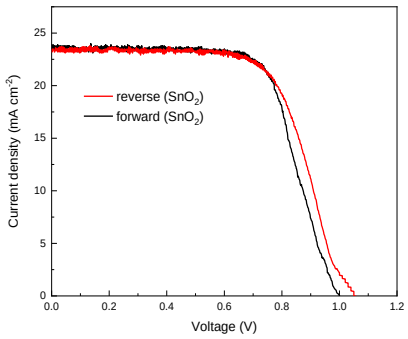

b)

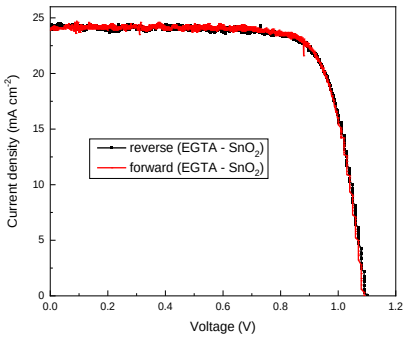

c)

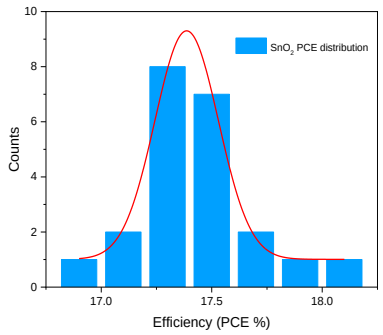

d)

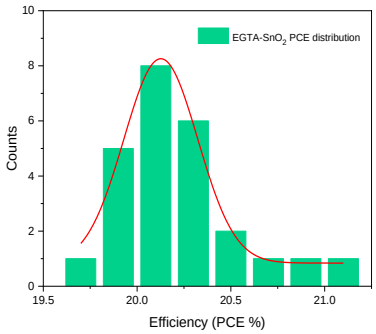

e)

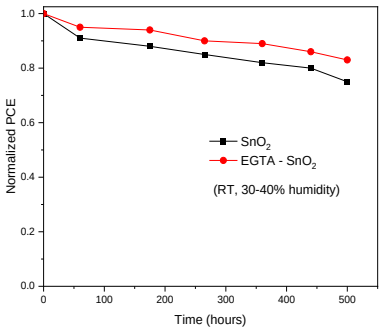

f)

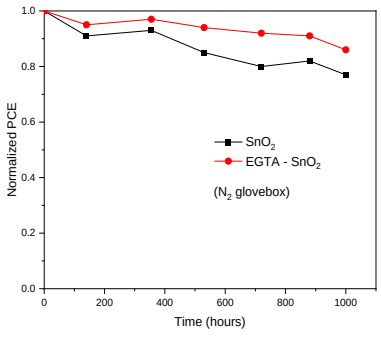

Figure 2.5. Forward and reverse J-V curves for (a) SnO_2 and (b) EGTA-SnO_2 based PSCs; PCE distribution of 30 devices for (c) SnO_2 and (d) EGTA-SnO_2 ETL-based PSCs; Normalized PCE of PSC devices stored in N_2 glovebox in 1000 h period; Normalized PCE of PSC devices stored in ambient conditions in 500 h period

Table 1. Photovoltaic performance parameters from *J-V* curves of PSCs regular SnO_2 and EGTA complex ETL

ETL	J_{sc} (mA cm^{-2})		V_{oc} (V)		FF		PCE (%)	
	Best	Average	Best	Average	Best	Average	Best	Average
SnO_2	21.66	20.48	1.08	1.06	0.80	0.75	18.63	17.40
EGTA-SnO_2 (0.26 mg/ml)	23.78	21.89	1.09	1.08	0.81	0.8	21.14	20.1

Table 2. Photovoltaic performance parameters from *J-V* curves of PSCs with different EGTA-SnO_2 concentrations. (Where 0.13, 0.26, 0.39 mg/ml are EGTA concentration in SnO_2)

EGTA conc.	J_{sc} (mA cm^{-2})		V_{oc} (V)		FF		PCE (%)	
	Best	Average	Best	Average	Best	Average	Best	Average
0.13 mg/ml	23.41	21.67	1.08	1.07	0.78	0.75	19.5	18.19
0.26 mg/ml	23.78	21.89	1.09	1.08	0.81	0.8	21.14	20.1
0.39 mg/ml	23.60	21.60	1.09	1.08	0.81	0.75	20.37	19.48

2.3. CONCLUSION

In conclusion, the EGTA-SnO_2 ETL formed by the complexation of SnO_2 with EGTA showed improved electrical conductivity and other properties compared to the SnO_2 ETL. The perovskite layer grown on the EGTA-SnO_2 ETL also showed larger grains, fewer grain boundaries, higher crystallinity, and lower trap density. As a result, the efficiency of the PSCs based on the EGTA-SnO_2 ETL significantly increased from 18.63% to 21.14% for the SnO_2 ETL-based device, with large improvements in all 3 key parameters, Jsc, Voc, and FF. In addition, after 500 h of exposure to ambient conditions, the unencapsulated PSCs based on the EGTA-SnO_2 ETL only dropped by 20%, which has also improved compared to the device based on the SnO_2 ETL. The findings of this research showed that incorporating EGTA in the SnO_2 ETL has a positive impact on the conductivity of the ETL, the growth of the subsequent perovskite layer, and the performance of

the resulting perovskite solar cell. This study presents a straightforward method to enhance the properties of the SnO_2 ETL for fabricating PSCs with improved efficiency and stability.

Experimental section

Materials

ITO glass was purchased from Kintec. The SnO_2 colloid dispersion was purchased from Alfa Aesar (tin (IV) oxide, 15% in H_2O colloidal dispersion). Spiro-OMeTAD (*N*^{2},*N*^{2},*N*$^{2'}$,*N*$^{2'}$,*N*^{7},*N*^{7},*N*$^{7'}$,*N*$^{7'}$-octakis(4-methoxyphenyl)-9,9′-spirobi[9H-fluorene]-2,2′,7,7′-tetramine) was purchased from Xi'an Polymer Light Technology Corp. FAI (Formamidinium iodide), MAI (Methylammonium iodide), PbI_2 (Lead (IV) Iodide), EGTA (Ethylene glycol-bis(2-aminoethylether)-*N,N,N′,N′*-tetraacetic acid) and all chemicals, such as chlorobenzene (CB), N, N-dimethylformamide (DMF), and dimethyl sulfoxide (DMSO) were purchased from Sigma-Aldrich. All reagents used in this work were used as received.

Preparation of perovskite precursor

The 1.4 M $MA_{0.9}FA_{0.1}PbI_3$ precursor solution was prepared by dissolving 24, 200 and 645.5 mg of FAI, MAI, and PbI_2, in 1 mL of 0.9 mL DMF and 0.1 mL DMSO mixed solvents. The solution was stirred at room temperature for 6 h.

Preparation of SnO_2 and EGTA-SnO_2 precursor

EGTA with different masses were dissolved in 1 mL of deionized water respectively, and the SnO_2 aqueous colloidal dispersion (15 wt%) was diluted using deionized water to the concentration of 2.5 wt%. The SnO_2 and EGTA-SnO_2 solutions were stirred for 2 h at room temperature. The EGTA-SnO_2 precursor was prepared by mixing SnO_2 and EGTA solutions with a volume ratio of 1:1, then put on a hot plate at 80°C for 5 h under stirring conditions.

Methods

The ITO glasses were washed with deionized water, acetone, and isopropanol in the ultrasonic bath for 20 min. The pre-cleaned ITO glasses were dried with nitrogen flow and exposed to a UV ozone (UVO) illumination for 20 min. After that, The SnO_2 and EGTA-SnO_2 films were fabricated

by spin-coating onto the ITO substrates at 3500 rpm for 30 s, followed by thermal annealing at 150℃ for 30 min. The perovskite precursor solution was dripped onto the ITO/ETL substrates and spin-coated at 4000 rpm 35 s and at after 6 s, 70 μL toluene (as anti-solvent) was quickly injected onto the substrate. Then, the perovskite films were transferred onto a hotplate annealing at 100◦C for 15 min. After, the Spiro-OMeTAD solution was coated on perovskite films at 3500 rpm for 30 s with an accelerated speed of 2000 rpm. The 1-mL Spiro-OMeTAD chlorobenzene solution contains 73.5 mg of Spiro-OMeTAD, 29 μL of 4-tert-butylpyridine, and 17 μL of lithium bis (trifluoromethylsulfonyl) imide of 520 mg mL^{-1} in acetonitrile. Finally, MoO_3/Ag electrodes with a thickness of 10 and 100 nm were deposited under a high vacuum. The perovskite solar cells were fabricated with an effective area of 0.052 cm^2.

Characterizations

The J-V curve was measured using Agilent B2912A semiconductor Analyzer with Science Tech SLB300-A Solar Simulator. Each solar cell's active area is 0.0574 cm^2. The light source was A 450W xenon lamp with an air mass (AM) 1.5 filter. The X-Ray diffraction (XRD) measurements were conducted using a Bruker D8 Advance diffractometer with Cu Ka radiation (l = 0.15418 nm) with the polymer films spin-coated onto dodecyltrichlorosilane modified $SiO_2/p^{++}Si$ substates annealed at different temperatures. Atomic force microscopy (AFM) images were taken using a Dimension 3100 scanning probe microscope. AFM analysis was used the determination of the surface morphology and roughness of the thin film samples. The films used for AFM were spin-coated on a bare or dodecyltrichlorosilane modified $SiO_2/p^{++}Si$ substate. The UV-Visible-NIR spectroscopy measurements are conducted using a Thermo Scientific GENESYSTM 10S VIS spectrophotometer or using the Cary 7000 UMS UV-Vis-NIR spectrophotometer. The surface morphological characterizations of the perovskite films were performed by using scanning electron microscopy (SEM, Nova NanoSEM450) at a 10 kV accelerating voltage. The steady-state PL were measured under the excitation of a 473 nm pulsed laser with a power density of 15 μJ cm^{-2}, based on an FLS920 (Edinburgh Instruments) fluorescence spectrometer. A Micro Capture Pro coupled with Image J software was applied to obtain the water contact angles of the substrates.

CHAPTER 3

Passivation of perovskite solar cells with dicyanobenzene isomers

ABSTRACT

Aromatic Lewis bases are considered one of the most effective passivating materials used in perovskite solar cell fabrication that can drastically suppress non-radiative recombination and improve the efficiency and stability of perovskite solar cell devices. Herein, three isomers of dicyanobenzene (DCB) (1,2-DCB, 1,3-DCB, and 1,4-DCB) are used as weak Lewis base passivating reagents between perovskite and hole transport layers. Comparative interaction with residual PbI_2 in formed perovskite film demonstrated that 1,3-DCB can significantly reduce the presence of lead iodide which can negatively impact both efficiency and stability of devices. This is combined with a significant reduction in trap density and improved perovskite morphology, enhanced power conversion efficiency (PCE) of the planar perovskite solar cells of up to 21.07% with negligible hysteresis. In addition, passivation with DCB isomers makes PSCs more stable in ambient conditions, retaining nearly 90% of initial efficiency for over 600 h.

3.1 INTRODUCTION

Organometal halide-based Perovskite solar cells (PSCs) have invited significant academic interest due to numerous properties, including small exciton energy, long charge diffusion length, high tolerance to defects and band gap tunability [100]. The power conversion efficiency (PCE) of PSCs has already passed 25% [6] yet there are important issues that hinder PSCs from being a commercially viable alternative energy source. For instance, defects formed between grain boundaries (GBs) are due to the polycrystalline nature of solution-processed perovskite films, leading to photogenerated carrier recombination and further shortens the carrier lifetime [67,101,102]. In addition, these deficiencies encourage a quick perovskite degradation [103, 104] as they promote permeation of atmospheric water and oxygen and ion migration within the perovskite structure [67, 105]. Therefore, decreasing the number of defects or removing their negative impacts is required for PSCs to attain high performance and durability under ambient conditions [106, 107].

Two common ways to reduce the number of defects formed on the surface of the perovskite film are through bulk passivation and surface passivation. To bulk passivate a perovskite film, a passivator is added to the precursor solution so that during the formation and crystallization processes, the passivator can neutralize charged ionic defects [34, 108]. Alternatively, as many defects form on the surface of a film, a passivation layer can be spin-coated on top of the perovskite film [32, 109, 110]. This method, also called post-treatment surface modification, can be considered a more straightforward option since it does not alter the fabrication process of the perovskite layer. For instance, You et al. spin-coated a phenylethylammonium iodide (PEAI) solution, an organic molecule containing a π-conjugated phenyl ring, on top of the perovskite layer and reached a certified PCE of over 23% due to the improvement of charge transport, reduction of Pb^{2+} interstitials through amine coordination, and filling of iodide ion vacancies [67]. Cai et al. improved the overall PCE of PSCs up to 23.3% with increased operational stability over 1000 h through passivating the perovskite layer with 2-aminopyridine that can more gently stabilize the organic species in the perovskite in contrast to the 4-aminopyridine isomer with a higher level of basicity. The passivating layer consisting of 2-aminopyridine improves interfacial charge transport between perovskite and the hole transport layer by significantly reducing the formation of low-dimensional (2D) perovskite on top of formed, regular perovskite [111]. A wide range of compounds is used as the passivation of perovskite films, including organic small molecules [34, 67], polymers [112-115], and metal and organic halides [67, 116]. However, small organic molecules have the advantages of having a smaller size, high solubility, and good permeability that can easily permeate and interact with the perovskite film [34].

In this work, we used three dicyanobenzene (DCB) isomers, 1,2-DCB, 1,3-DCB, and 1,4-DCB, as a passivator layer between the perovskite and Spiro-OMeTAD hole transport layer. All three isomers are aromatic organic molecules with two electron-withdrawing –CN passivation functional groups featured in 1,2 (ortho), 1,3 (meta), and 1,4 (para)-positions in the benzene ring. As weak Lewis bases due to the lone electron pairs of both N atoms of the cyano group, DCB isomers can reduce Pb^{2+} interstitials through coordination with CN groups [117, 118] and filling vacancies that consequently reduce surface defects on the perovskite films [115]. Furthermore, electron-donating Lewis bases, through interaction with organic cations present in perovskite precursors (MA^+ and FA^+), can reduce the migration of H^+ ions from organic entities to passivator

alongside with previously mentioned passivation of vacant Pb^{2+} ions [119]. In addition, as reported by Roose et al., excess PbI_2 can also halt both the long-term operation of PSCs and further performance loss [120].

From an investigation of 1,2-DCB, 1,3-DCB, and 1,4-DCB, the 1,3-DCB isomer shows a significant reduction of lead iodide presence through the complex formation. Combined with effective passivation of both shallow- and deep-level defects, PSCs passivated with 1,3-DCB resulted in a PCE increase from 18.80 % for the control device to 21.07% for the passivated device with negligible hysteresis and retention of over 80% of initial efficiency for over 1000 h at ambient conditions. This work proposes a viable technique for increasing the performance of PSC by using DCB organic molecules and bringing some understanding regarding the impact of their isomerism in the passivation of perovskite film.

3.2. RESULTS AND DISCUSSION

The chemical structures of DCB isomers are presented in Figure 3.1 (a). To evaluate the interaction between PbI_2 and DCB isomers, equimolar solutions of PbI_2 and a mix of both PbI_2 and DCB isomers were prepared, and UV-Vis absorption spectra were measured (Figure 3.1 (b)). The UV-Vis spectrum of a PbI_2 solution in DMF (black line in Figure 3.1 (b)) shows two peaks at 275 and 323 nm, which correspond to PbI^+ or PbI_2 species or their complex combinations [121]. In Figure 3.1(b), for the solution of PbI_2 + 1,4-DCB, a new band at around 370 nm appeared, which may indicate the formation of other iodoplumbate complexes, especially iodine-rich, like PbI_3^- or PbI_4^{2-} [121, 122]. On the other hand, the absorption peaks of PbI_2 remained the strongest for the sample of 1,2-DCB + PbI_2 among the three isomers which indicates that the interaction of 1,2-DCB with PbI_2 is much weaker than 1,4-DCB and 1,3-DCB isomers. 1,3-DCB isomer shows medium interaction with PbI_2 retaining some free PbI_2. According to Roose et al., while an excess of PbI_2 present in the perovskite layer can lead to parasitic absorption, performance decrease and quick deterioration of the device, a modest amount of PbI_2 (<5 mol %) can increase short-circuit current (Jsc), enhance charge extraction, and improve cell performance [121].

XRD was used to confirm the influence of DCB isomer passivation on the crystal formation of the perovskite layer. Increased intensity of the XRD patterns at 14.1° corresponds to improved crystallinity (1,3-DCB > 1,4-DCB > 1,2-DCB > control). At a phase angle of 12.7°, the XRD peak intensity for PbI_2 dropped in the same order as in UV-vis above spectra (1,4-DCB > 1,3-DCB > 1,2-DCB) confirming interactions between PbI_2 and DCB isomers. To evaluate the influence that the DCB isomers passivation layer has on the surface morphology of the perovskite films, scanning electron microscopy (SEM) and atomic force microscopy (AFM) were utilized. The top-view SEM images of both treated and non-treated perovskite films are shown in Figure 3.1 (d). DCB isomer passivated $MAFAPbI_3$ perovskite films exhibited less clear grain boundaries and compact formation than unmodified $MAFAPbI_3$ perovskite films. As a result of reduced grain boundaries, a smaller number of defects formed, which in turn suppresses the nonradiative charge recombination. Figure 3.1 (e) shows the AFM images of the untreated and DCB isomer-treated perovskite films. The measured root-mean-square (RMS) surface roughness decreased from 59.5 nm for pure perovskite film to 42.2, 37.3, and 40.5 nm for 1,2-DCB, 1,3-DCB, and 1,4-DCB passivated surfaces, respectively, representing a significant decrease in surface roughness. Consequently, the passivated layer is in a better position to make effective contact with the HTL because of the smoother surface of the perovskite film, which improves the processes of hole separation and transportation.

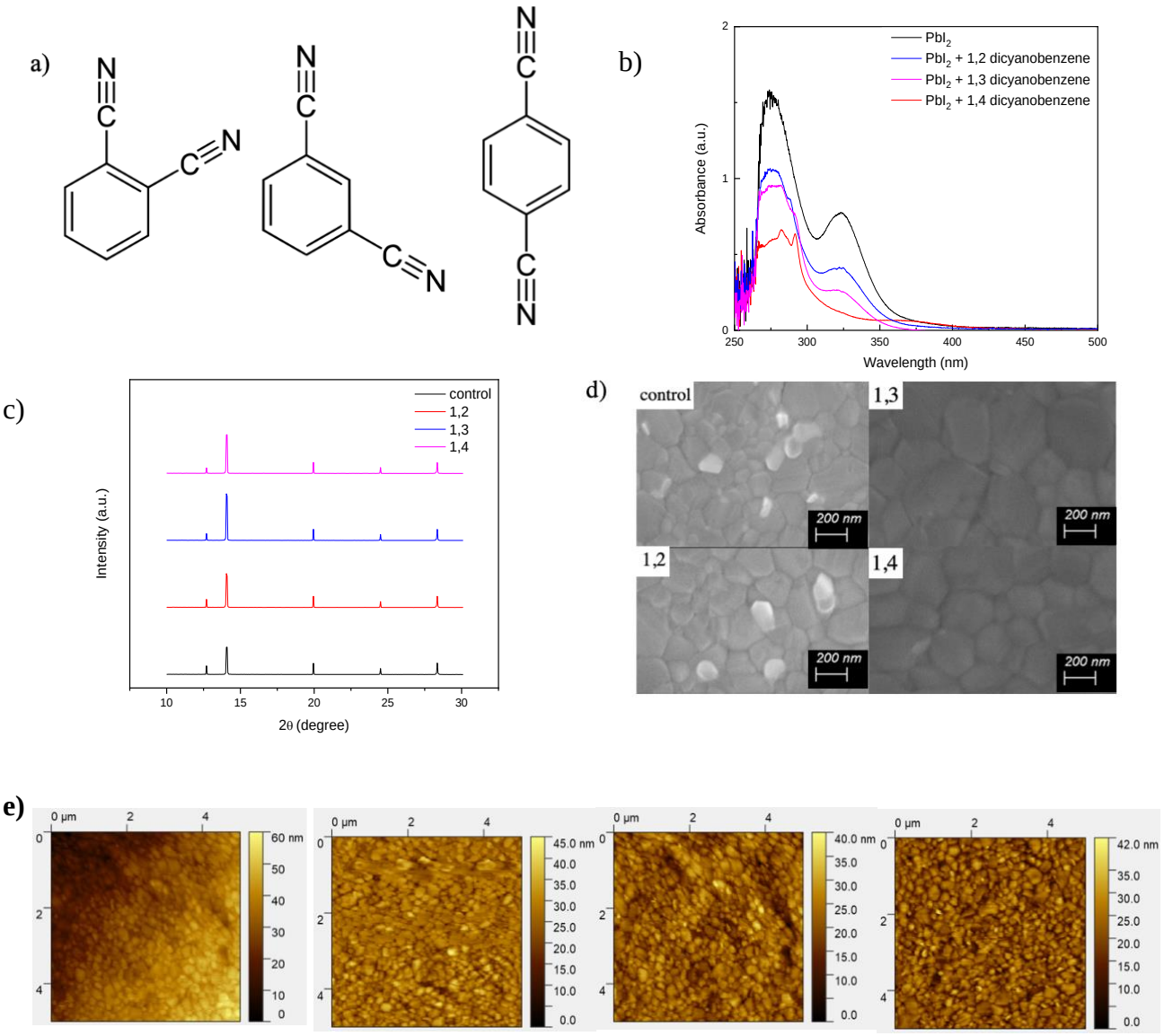

Figure 3.1. (a) chemical structure of 1,2-DCB, 1,3-DCB, and 1,4-DCB from left to right; (b) UV-Vis spectra of PbI_2, 1:1 equimolar ratio of 1,2-DCB + PbI_2, 1,3-DCB + PbI_2, 1,4-DCB + PbI_2, (c) XRD spectra of control (untreated) and treated with 1,2-DCB, 1,3-DCB, and 1,4-DCB; (d) SEM pictures of control (untreated) and treated with 1,2-DCB, 1,3-DCB, and 1,4-DCB perovskite films; e) AFM pictures of control (untreated) and treated with 1,2-DCB, 1,3-DCB, and 1,4-DCB perovskite films.

3.2.1. Optical Parameters

The optical characteristics of the perovskite films were investigated by using UV-Vis absorption and photoluminescence (PL) spectroscopies, and the results are shown in Figures 3.2 (a) and (b). In Figure 3.2 (a), it can be seen that both passivated and unpassivated perovskite films have roughly the same absorption spectrum. This indicates that treatment with all three DCB isomers had negligible influence on the perovskite's ability to absorb light and its optical band gap. Moreover, PL spectra were examined using treated and untreated perovskite films prepared on non-conductive glass substrates (Figure 3.2 (b)). After treating the perovskite layer with DCB isomers, PL intensities significantly increased compared to non-treated perovskite film. The 1,3-DCB treated sample showed the most prominent peak, followed by the 1,4-DCB, 1,2-DCB treated and control samples. This indicates that recombination in the perovskite layer passivated with DCB had been considerably suppressed [123,124]. To gain further understanding of the effect that DCB passivation has on the defect state density in the perovskite films, the trap densities (N_t) of devices with and without passivation with DCB isomers were measured by the space-charge-limited current (SCLC) method. Electron-only devices (ITO/SnO_2/perovskite/PCBM/Ag and ITO/SnO_2/Perovskite/DCB isomer/PCBM/Ag) were fabricated and the results are shown in Figure 3.2 (c). Using the trap-filled limit voltage (V_{TFL}) of each sample, N_t can be calculated by using Equation (5):

$$N_{\mathrm{t}} = \frac{2\varepsilon_0 \varepsilon V_{\mathrm{TFL}}}{eL^2}$$

V_{TFL} (trap-filled limit voltage) is the inflection point on the I–V curve of the trap-filled limit region and represents that carrier injection filled all the trap states [125], L is the thickness of the perovskite film, e is the elementary charge, e is the relative dielectric constant of the perovskite, and ε_0 is the vacuum permittivity [126–128]. The V_{TFL} of each perovskite film was obtained through the inflection point on the I–V curve, which reflects that the trap state is filled by carrier injection [129]. The N_t (electron) values for the control, 1,2-DCB, 1,3-DCB, and 1,4-DCB passivated films are 1.34×10^{16} and 9.38×10^{15} cm^3, 8.68×10^{15} cm^3, 9.21×10^{15} cm^3 (Fig. 3.2 (c)-(f)), accordingly. The fact that the trap state density was greatly decreased suggests that all three isomers, especially the 1,3-DCB isomer can efficiently reduce the traps present in the perovskite films.

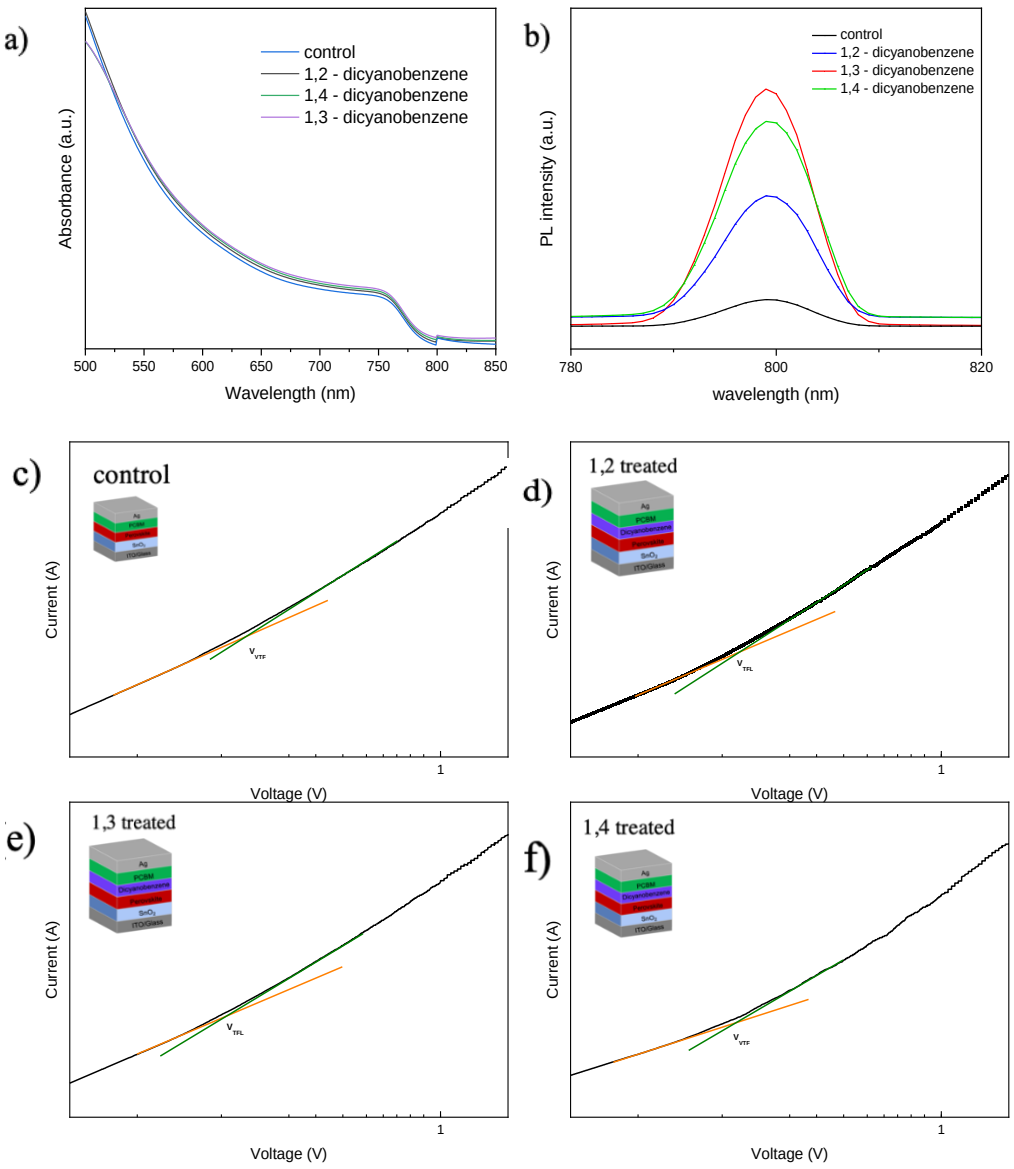

Figure 3.2. (a) UV-Vis absorption spectra for control, cyanobenzene treated perovskite films; (b) PL spectra of ITO/Perovskite and ITO/Perovskite/DCB isomer structures; (c) – (f) perovskite films passivated using DCB passivation layer; dark I–V curves of the hole-only devices (c) without and (d) 1,2-DCB treated; (e) 1,3-DCB treated and (f) 1,4-DCB treated devices.

3.2.2. PSCs Performance

PSCs based on DCB isomers as passivation agents were fabricated using a cell configuration of ITO/SnO_2/($MA_{0.9}FA_{0.1}PbI_3$)/DCB isomer/Spiro-OMeTAD/MoO_3/Ag and compared to the regular structure (Fig 3.3 (a)). The current density–voltage (J–V) curves of the cells passivated with three isomers of DCB both in forward and reverse scans are shown in Fig. 3.3 (c) – (f), and the performance characteristics depending on the concentration of each isomer that was derived from the J–V curves are included in Table 3-6. The hysteresis index (HI) of the device passivated by DCB isomers drops to negligible levels compared to control PSC, suggesting that the hysteresis impact of devices considerably decreased due to the presence passivation layer. The control cell without any passivation layer has the highest PCE of 18.8%. In contrast, the PCE of treated devices was generally higher, with a champion efficiency of 21.07% achieved with 2 mg/mL 1,3-DCB treatment. Open circuit voltage (Voc) and fill factor (FF) were the main driver for improved efficiency of devices, as the average PCE for 35 devices increased from 17.60% to 19.87% via passivation with 1,3-DCB (for 1,2-DCB - 18.44% and 1,4-DCB - 19.56%). PSCs with and without DCB passivation are compared statistically and show good reproducibility (Fig. 3,3 (g)-(j)). Figure 3.3 (b) depicts the impact of all three dicyanoisomers' passivation on the external quantum efficiency (EQE) and integrated Jsc of the PSCs. In the visible wavelength range of 370 to 760 nm, the EQE of PSCs that has been passivated with DCB isomers is greater than that of an unpassivated device, which is an indicator of an increased photo-generated carrier density.

Table 3. Photovoltaic performance parameters from *J-V* curves of PSCs without and with different DCB isomer passivation

Passivation layer	J_{sc} (mA cm^{-2})		V_{oc} (V)		FF		PCE (%)	
	Best	Average	Best	Average	Best	Average	Best	Average
w/o	21.89	21.25	1.07	1.06	0.80	0.75	18.33	17.60
1,2-DCB (2 mg/ml)	22.06	21.89	1.08	1.07	0.81	0.80	19.24	18.44
1,3-DCB (2 mg/ml)	22.80	22.23	1.09	1.08	0.83	0.82	21.07	19.87
1,4-DCB (2 mg/ml)	23.18	22.07	1.09	1.08	0.82	0.81	20.28	19.56

Table 4. Photovoltaic performance parameters from *J-V* curves of PSCs with different 1,2-DCB passivation concentrations.

1,2-DCB conc.	J_{sc} (mA cm^{-2})		V_{oc} (V)		FF		PCE (%)	
	Best	Average	Best	Average	Best	Average	Best	Average
w/o	21.28	21.20	1.07	1.05	0.80	0.77	18.33	17.59
1 mg/ml	23.41	21.89	1.07	1.06	0.78	0.75	18.86	18.21
2 mg/ml	22.06	21.89	1.08	1.07	0.81	0.80	19.24	18.44
4 mg/ml	21.65	22.90	1.08	1.04	0.81	0.75	19.12	18.15

Table 5. Photovoltaic performance parameters from *J-V* curves of PSCs with different 1,3-DCB passivation concentrations.

1,3-DCB conc.	J_{sc} (mA cm^{-2})		V_{oc} (V)		FF		PCE (%)	
	Best	Average	Best	Average	Best	Average	Best	Average
w/o	21.23	20.37	1.06	1.06	0.80	0.77	18.12	17.44
1 mg/ml	22.34	21.73	1.07	1.06	0.80	0.79	19.14	18.61
2 mg/ml	22.80	22.23	1.09	1.08	0.83	0.82	21.07	19.87
4 mg/ml	22.23	22.18	1.07	1.07	0.83	0.80	20.02	19.08

Table 6. Photovoltaic performance parameters from *J-V* curves of PSCs with different 1,4-DCB passivation concentrations.

1,4-DCB conc.	J_{sc} (mA cm^{-2})		V_{oc} (V)		FF		PCE (%)	
	Best	Average	Best	Average	Best	Average	Best	Average
w/o	21.89	21.08	1.07	1.05	0.77	0.75	18.25	17.60
1 mg/ml	21.42	21.01	1.08	1.06	0.82	0.80	19.49	18.35
2 mg/ml	23.18	22.07	1.09	1.08	0.82	0.81	20.28	19.56
4 mg/ml	22.30	22.21	1.08	1.06	0.82	0.80	20.10	18.91

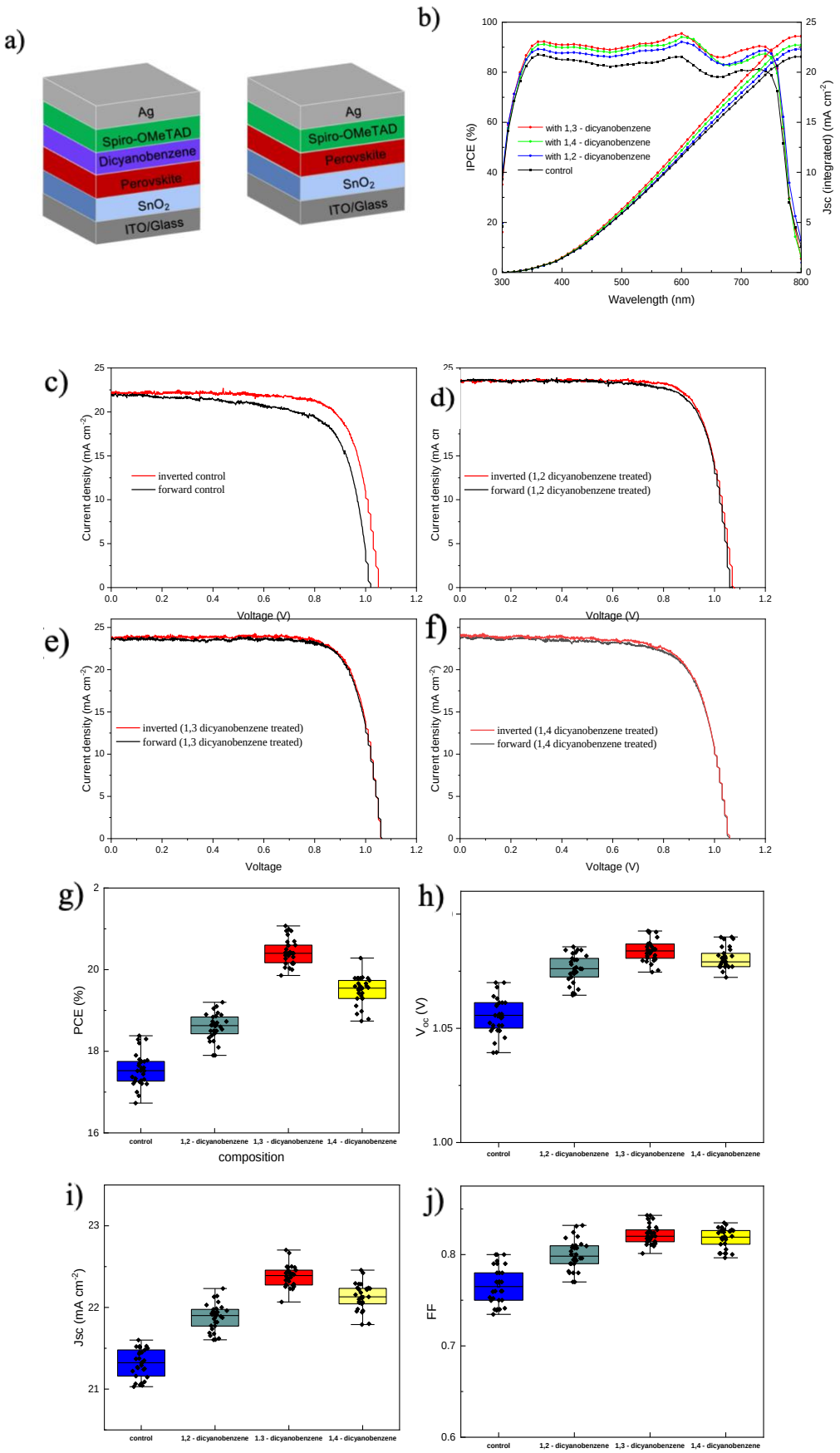
a)
Ag
Spiro-OMeTAD
Dicyanobenzene
Perovskite
SnO2
ITO/Glass
Ag
Spiro-OMeTAD
Perovskite
SnO2
ITO/Glass
b)
IPCE (%)
Jsc (integrated) (mA cm-2)
Wavelength (nm)
with 1,3 - dicyanobenzene
with 1,4 - dicyanobenzene
with 1,2 - dicyanobenzene
control
c)
Current density (mA cm-2)
Voltage (V)
inverted control
forward control
d)
Current density (mA cm
Voltage (V)
inverted (1,2 dicyanobenzene treated)
forward (1,2 dicyanobenzene treated)
e)
Current density (mA cm-2)
Voltage
inverted (1,3 dicyanobenzene treated)
forward (1,3 dicyanobenzene treated)
f)
Current density (mA cm-2)
Voltage (V)
inverted (1,4 dicyanobenzene treated)
forward (1,4 dicyanobenzene treated)
g)
PCE (%)
control
1,2 - dicyanobenzene
1,3 - dicyanobenzene
1,4 - dicyanobenzene
composition
h)
Voc (V)
control
1,2 - dicyanobenzene
1,3 - dicyanobenzene
1,4 - dicyanobenzene
i)
Jsc (mA cm-2)
control
1,2 - dicyanobenzene
1,3 - dicyanobenzene
1,4 - dicyanobenzene
j)
FF
control
1,2 - dicyanobenzene
1,3 - dicyanobenzene
1,4 - dicyanobenzene

Figure 3.3. (a) Structure for both passivated and control devices; (b) EQE spectra of control, 1,2-DCB, 1,3-DCB, and 1,4-DCB passivated PSCs; (c) – (f) J-V curves of control, 1,2-DCB, 1,3-DCB, and 1,4-DCB passivated PSCs; (g) Jsc, (h) Voc, (i) FF, (j) PCE distribution for the control, 1,2-DCB, 1,3-DCB, and 1,4-DCB passivated PSCs.

3.2.3. Stability

The PCE changes of control and passivated PSCs stored in an N_2-filled glovebox and (b) in ambient conditions are shown in Fig. 3.4 (a). It is evident that the PSC passivated with DCB has greater stability than the one without a passivation layer. Specifically, after 600 h of storage, the PSC with the DCB layer retained over 80% of its original efficiency, whereas the PSC without DCB passivation lost more than 20% of initial efficiency. The PSC performance degradation may be caused by the degradation of the perovskite layer, as well as the ion transfer produced by ambient moisture and oxygen [130]. Additionally, moisture tends to penetrate and react faster at grain boundaries that are more abundant in untreated devices [78]. The water contact angle on the perovskite film that was treated with the best-performing 1,3-DCB layer (83^o) is greater than that on the film that has not been treated (61^o) (Figure 3.4 (c) and (d)). This indicates that an increased hydrophobicity of the film surface can be obtained by treating the film with DCB isomers. Therefore, increased hydrophobicity, decreased trap density and reduced grain boundaries are considered responsible for the improved stability of the PSCs passivated with DCB.

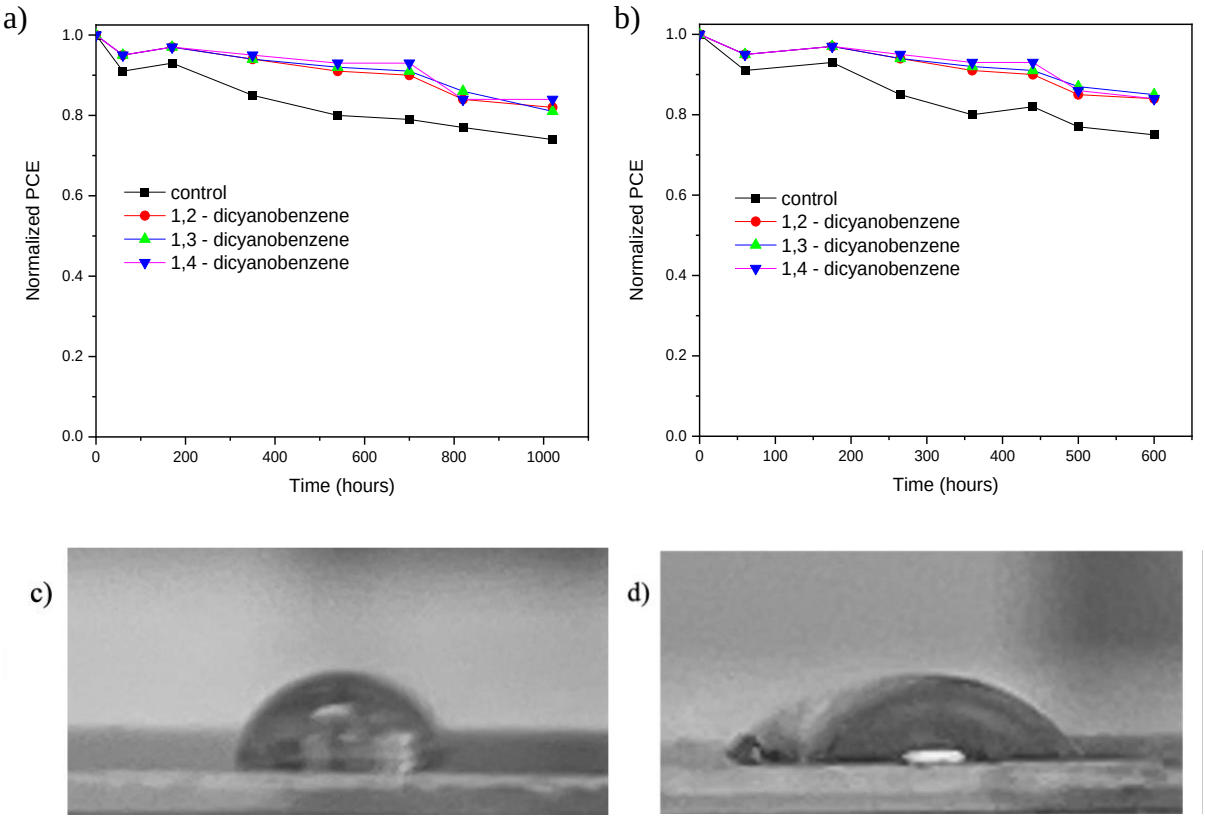

Figure 3.4. (a) Normalized PCE over time for devices stored in nitrogen glovebox; (b) normalized PCE over time for devices stored in ambient conditions; contact angles of (c) 1,3-DCB passivated, (d) unpassivated control devices.

3.3. CONCLUSION

In conclusion, we have demonstrated an effective passivation strategy to modify the perovskite film surface by introducing DCB isomers containing two cyano groups (–CN) and investigated its effects on the surface morphology and defect state density of the perovskite films as well as their photovoltaic performance. Functional groups of DCB interact with the present excess PbI_2 ions connected to both the PCE and stability performances of PSCs. While excess PbI_2 is detrimental, a small amount can be beneficial for crystal formation processes of the perovskite layer. Thus, the presence of a modest PbI_2 amount can be the best condition for retaining stability and efficiency yet still beneficially affecting the crystallinity of the perovskite layer. 1,4-DCB isomer forms more complexes with PbI_2 while demonstrating a little effect on the crystallinity of perovskite, while the

1,2-DCB isomer produces a weaker complex with residual PbI_2. 1,3-DCB isomer forming complexes and leaving some amount of PbI_2 comes closer to the aforementioned modest presence of PbI_2, reaching 21.07% efficiency and highest average efficiency at 19.87% compared to the regular average of 17.60%. In addition, as a direct result of DCB passivation processes, the perovskite layer improved moisture resistance, contributing to the device's improved long-term environmental stability. After 600 h of operation in ambient conditions, DCB-treated PSCs retain around 90% without encapsulation. This effective DCB isomers-based surface passivation presents a promising technique for boosting PSCs' efficiency and environmental stability.

Experimental section

Materials

ITO glass was purchased from Kintec. The SnO_2 colloid dispersion was purchased from Alfa Aesar (tin (IV) oxide, 15% in H_2O colloidal dispersion). Spiro-OMeTAD (*N*^{2},*N*^{2},*N*$^{2'}$,*N*$^{2'}$,*N*^{7},*N*^{7},*N*$^{7'}$,*N*$^{7'}$-octakis(4-methoxyphenyl)-9,9′-spirobi[9H-fluorene]-2,2′,7,7′-tetramine) was purchased from Xi'an Polymer Light Technology Corp. FAI (Formamidinium iodide), MAI (Methylammonium iodide), PbI_2 (Lead (IV) Iodide), 1,2- 1,3- and 1,4-dicyanobenzene and all chemicals, such as chlorobenzene (CB), N, N-dimethylformamide (DMF), and dimethyl sulfoxide (DMSO) were purchased from Sigma-Aldrich. All reagents used in this work were used as received.

Preparation of perovskite precursor

The 1.4 M $MA_{0.9}FA_{0.1}PbI_3$ precursor solution was prepared by dissolving 24, 200 and 650 mg of FAI, MAI, and PbI_2, in 1 mL of 0.9 mL DMF and 0.1 mL DMSO mixed solvents. The solution was stirred at room temperature for 6 h.

Preparation of dicyanobenzene isomer solutions

Dicyanobenzene isomers with different masses were dissolved in 1 mL of chlorobenzene respectively and left to stir for 1 h without heating.

Methods

The ITO glasses were washed with deionized water, acetone, and isopropanol in the ultrasonic bath for 20 min. The pre-cleaned ITO glasses were dried with nitrogen flow and exposed to a UV ozone (UVO) illumination for 20 min. After that, The SnO_2 and EGTA-SnO_2 films were fabricated by spin-coating onto the ITO substrates at 3500 rpm for 30 s, followed by thermal annealing at 150°C for 30 min. The perovskite precursor solution was dripped onto the ITO/ETL substrates and spin-coated at 4000 rpm 35 s. After 6 s, 70 μL toluene (as anti-solvent) was quickly injected onto the substrate. Then, the perovskite films were transferred onto a hotplate annealing at 100◦C for 15 min. This is followed by spin coating 40 μL of dicyanobenzene isomer solution at 3500 rpm for 30 s, followed by annealing at 100C for 10 min. After, the Spiro-OMeTAD solution was coated on perovskite films at 3500 rpm for 30 s with an accelerated speed of 2000 rpm. The 1-mL Spiro-OMeTAD chlorobenzene solution contains 73.5 mg of Spiro-OMeTAD, 29 μL of 4-tert-butylpyridine, and 17 μL of lithium bis (trifluoromethylsulfonyl) imide of 520 mg mL− 1 in acetonitrile. Finally, MoO_3/Ag electrodes with 10 and 100 nm thickness were deposited under a high vacuum. The perovskite solar cells were fabricated with an effective area of 0.052 cm^2. To conduct the UV-Vis absorption experiment for PbI_2 + dicyanobenzene isomers, an equimolar (0.1M) solution of PbI_2 and PbI_2 with each dicyanoisomers mixed in DMF.

Characterizations

The J-V curve was measured using Agilent B2912A semiconductor Analyzer with Science Tech SLB300-A Solar Simulator. Each solar cell's active area is 0.0574 cm^2. The light source was A 450W xenon lamp with an air mass (AM) 1.5 filter. The X-Ray diffraction (XRD) measurements were conducted using a Bruker D8 Advance diffractometer with Cu Ka radiation (l = 0.15418 nm) with the polymer films spin-coated onto dodecyltrichlorosilane modified SiO_2/p++Si substates annealed at different temperatures. Atomic force microscopy (AFM) images were taken using a Dimension 3100 scanning probe microscope. AFM analysis has used the determination of the surface morphology and roughness of the thin film samples. The films used for AFM were spin-coated on a bare or dodecyltrichlorosilane modified SiO_2/p++Si substate. The UV-Visible-NIR spectroscopy measurements are conducted using a Thermo Scientific GENESYSTM 10S VIS spectrophotometer or the Cary 7000 UMS UV-Vis-NIR spectrophotometer. The surface morphological characterizations of the perovskite films were performed using scanning electron

microscopy (SEM, Nova NanoSEM450) at a 10 kV accelerating voltage. The steady-state PL was measured under the excitation of a 473 nm pulsed laser with a power density of 15 μJ cm^2, based on an FLS920 (Edinburgh Instruments) fluorescence spectrometer. A Micro Capture Pro coupled with Image J software was applied to obtain the water contact angles of the substrates.

CHAPTER 4

Summary and Future Direction

In conclusion, this thesis presents a comprehensive, multifunctional approach to tackling various challenges that PSCs device fabrication currently faces, especially the formation of layers and interlayers in its device structure. The PSC device performance and overall stability were characterized and analyzed to give a complete picture of the processes happening between and inside the charge transport layers and perovskite layer.

In chapter 2, the formation of the complex between SnO_2 and EGTA increased ETL's conductivity and other fundamental properties. As a direct consequence, the efficiency of the PSCs that use EGTA-SnO_2 as ETL shows a considerable increase, rising from 18.63% to 21.14%, along with a significant improvement in each of the three key parameters (Jsc, Voc, FF). In addition, the unencapsulated PSCs carrying EGTA-SnO_2 only degrade by a factor of 20% despite being subjected to the conditions of the surrounding environment for over 500 h. This research work demonstrates a clear and straightforward method for increasing the performance of SnO_2 film to build perovskite devices that are efficient as well as stable. In further research, a molecule analogous to an acid-base organic complex might be employed in a ZnO solution that is a less expensive and more conducive ETL alternative that is already extensively used in the manufacturing of organic solar cells. Because of the high basicity and reactivity of the ZnO layer, its incorporation in PSCs represents a challenge as the perovskite layer interacts strongly with ZnO. That’s why it is necessary to find a small, suitable organic acid capable of forming a complex with the Zn^{2+} ion, neutralizing the pH of the ZnO layer and forming stable PSC device.

In chapter 3, our results show that incorporating DCB isomers with two cyano groups (–CN) as a passivation layer may effectively improve the perovskite film surface while examining the impacts on the surface morphology and defect state density of the perovskite films' photovoltaic efficiency. 1,3-DCB isomer forms complex and leaves some amount of PbI_2 produces 21.07% efficiency and the highest average efficiency at 19.87% compared to regular 17.60% efficiency. In addition, the perovskite layer's resistance to moisture was significantly increased due to the DCB passivation procedures. This, in turn, contributed to the improved environmental stability of the device. PSCs

treated with DCB have an efficiency retention rate of around 90% without encapsulation after 600 h of operation in ambient settings. This efficient surface passivation based on DCB isomers is a potential strategy for increasing PSCs' efficiency and environmental stability. Further work may be done to understand the complicated interaction processes of other small organic Lewis bases with various functional groups and their isomers with perovskite and different charge transport layers. In this approach, we will be able to get knowledge of the passivation processes that are taking place on the surfaces and arrive at a method that is both more effective and less toxic for increasing the PSCs' stability over a commercially viable period.

References:

[1] - Saikia, D., Betal, A., Bera, J., & Sahu, S. (2022). Progress and challenges of halide perovskite-based solar cell- A brief review. *Materials Science in Semiconductor Processing*, *150*, 106953. https://doi.org/10.1016/j.mssp.2022.106953

[2] - Manser, J. S., Christians, J. A., & Kamat, P. V. (2016). Intriguing optoelectronic properties of metal halide perovskites. *Chemical Reviews*, *116*(21), 12956–13008. https://doi.org/10.1021/acs.chemrev.6b00136

[3] - Cheng, Z., & Lin, J. (2010). Layered organic-inorganic hybrid perovskites: Structure, optical properties, film preparation, patterning and templating engineering. *CrystEngComm*, *12*(10), 2646. https://doi.org/10.1039/c001929a

[4] - Kojima, A., Teshima, K., Shirai, Y., & Miyasaka, T. (2009). Organometal halide perovskites as visible-light sensitizers for photovoltaic cells. *Journal of the American Chemical Society*, *131*(17), 6050–6051. https://doi.org/10.1021/ja809598r

[5] - Kim, H.-S., Lee, C.-R., Im, J.-H., Lee, K.-B., Moehl, T., Marchioro, A., Moon, S.-J., Humphry-Baker, R., Yum, J.-H., Moser, J. E., Grätzel, M., & Park, N.-G. (2012). Lead iodide perovskite sensitized all-solid-state submicron thin film mesoscopic solar cell with efficiency exceeding 9%. *Scientific Reports*, *2*(1). https://doi.org/10.1038/srep00591

[6] - *Best research-cell efficiency chart*. NREL.gov. (n.d.). Retrieved July 30, 2022, from https://www.nrel.gov/pv/cell-efficiency.html

[7] - Hoppe, H., & Sariciftci, N. S. (2004). Organic Solar Cells: An overview. *Journal of Materials Research*, *19*(7), 1924–1945. https://doi.org/10.1557/jmr.2004.0252

[8] - Rafique, S., Abdullah, S. M., Sulaiman, K., & Iwamoto, M. (2018). Fundamentals of bulk heterojunction organic solar cells: An overview of stability/degradation issues and strategies for improvement. *Renewable and Sustainable Energy Reviews*, *84*, 43–53. https://doi.org/10.1016/j.rser.2017.12.008

[9] - Troshin, P. A., Lyubovskaya, R. N., & Razumov, V. F. (2008). Organic Solar Cells: Structure, materials, critical characteristics, and outlook. *Nanotechnologies in Russia*, *3*(5-6), 242–271. https://doi.org/10.1134/s1995078008050029

[10] - Fung, D. D., & Choy, W. C. (2012). Introduction to organic solar cells. *Organic Solar Cells*, 1–16. https://doi.org/10.1007/978-1-4471-4823-4_1

[11] - Elumalai, N. K., & Uddin, A. (2016). Open circuit voltage of organic solar cells: An in-depth review. *Energy & Environmental Science*, *9*(2), 391–410. https://doi.org/10.1039/c5ee02871j

[12] - Qi, B., & Wang, J. (2012). Open-circuit voltage in organic solar cells. *Journal of Materials Chemistry*, *22*(46), 24315. https://doi.org/10.1039/c2jm33719c

[13] - Chandrasekaran, J., Nithyaprakash, D., Ajjan, K. B., Maruthamuthu, S., Manoharan, D., & Kumar, S. (2011). Hybrid solar cell based on blending of organic and inorganic materials—an Overview. *Renewable and Sustainable Energy Reviews*, *15*(2), 1228–1238. https://doi.org/10.1016/j.rser.2010.09.017

[14] - Trukhanov, V. A., Bruevich, V. V., & Paraschuk, D. Y. (2015). Fill factor in organic solar cells can exceed the Shockley-Queisser limit. *Scientific Reports*, *5*(1). https://doi.org/10.1038/srep11478

[15] - Qi, B., & Wang, J. (2013). Fill factor in organic solar cells. *Physical Chemistry Chemical Physics*, *15*(23), 8972. https://doi.org/10.1039/c3cp51383a

[16] - Cui, J., Yuan, H., Li, J., Xu, X., Shen, Y., Lin, H., & Wang, M. (2015). Recent progress in efficient hybrid lead halide perovskite solar cells. *Science and Technology of Advanced Materials*, *16*(3), 036004. https://doi.org/10.1088/1468-6996/16/3/036004

[17] - Mandati, S., Dileep. k, R., Veerappan, G., & Ramasamy, E. (2022). Large area bar coated TiO_2 electron transport layers for perovskite solar cells with excellent performance homogeneity. *Solar Energy*, *240*, 258–268. https://doi.org/10.1016/j.solener.2022.04.060

[18] - Cao, J., Lv, X., Zhang, P., Chuong, T. T., Wu, B., Feng, X., Shan, C., Liu, J., & Tang, Y. (2018). Plant Sunscreen and Co(II)/(III) porphyrins for UV-resistant and thermally stable perovskite solar cells: From natural to artificial. *Advanced Materials*, *30*(27), 1800568. https://doi.org/10.1002/adma.201800568

[19] - Jeon, N. J., Na, H., Jung, E. H., Yang, T.-Y., Lee, Y. G., Kim, G., Shin, H.-W., Il Seok, S., Lee, J., & Seo, J. (2018). A fluorene-terminated Hole-transporting material for highly efficient and stable perovskite solar cells. *Nature Energy*, *3*(8), 682–689. https://doi.org/10.1038/s41560-018-0200-6

[20] - Ball, J. M., Lee, M. M., Hey, A., & Snaith, H. J. (2013). Low-temperature processed meso-superstructured to thin-film perovskite solar cells. *Energy & Environmental Science*, *6*(6), 1739. https://doi.org/10.1039/c3ee40810h

[21] - Wojciechowski, K., Saliba, M., Leijtens, T., Abate, A., & Snaith, H. J. (2014). Sub-150 °C processed meso-superstructured perovskite solar cells with enhanced efficiency. *Energy Environ. Sci.*, *7*(3), 1142–1147. https://doi.org/10.1039/c3ee43707h

[22] - Makableh, Y. F., Hassan, W., Awad, I. A., & Aljaiuossi, G. (2021). Comprehensive Electrical Modeling Analysis of heterojunction perovskite solar cells by using different electron transport nanostructured layers. *Superlattices and Microstructures*, *150*, 106777. https://doi.org/10.1016/j.spmi.2020.106777

[23] - Snaith, H. J., Abate, A., Ball, J. M., Eperon, G. E., Leijtens, T., Noel, N. K., Stranks, S. D., Wang, J. T.-W., Wojciechowski, K., & Zhang, W. (2014). Anomalous hysteresis in perovskite solar cells. *The Journal of Physical Chemistry Letters*, *5*(9), 1511–1515. https://doi.org/10.1021/jz500113x

[24] – Anaraki, E. H., Kermanpur, A., Steier, L., Domanski, K., Matsui, T., Tress, W., Saliba, M., Abate, A., Grätzel, M., Hagfeldt, A., & Correa-Baena, J.-P. (2016). Highly efficient and stable planar perovskite solar cells by solution-processed tin oxide. *Energy & Environmental Science*, *9*(10), 3128–3134. https://doi.org/10.1039/c6ee02390h

[25] - Ahn, N., Kwak, K., Jang, M. S., Yoon, H., Lee, B. Y., Lee, J.-K., Pikhitsa, P. V., Byun, J., & Choi, M. (2016). Trapped charge-driven degradation of perovskite solar cells. *Nature Communications*, *7*(1). https://doi.org/10.1038/ncomms13422

[26] - Yin, X., Song, Z., Li, Z., & Tang, W. (2020). Toward Ideal Hole Transport Materials: A review on recent progress in Dopant-free hole transport materials for fabricating efficient and stable perovskite solar cells. *Energy & Environmental Science*, *13*(11), 4057–4086. https://doi.org/10.1039/d0ee02337j

[27] - Dawson, J. A., Naylor, A. J., Eames, C., Roberts, M., Zhang, W., Snaith, H. J., Bruce, P. G., & Islam, M. S. (2017). Mechanisms of lithium intercalation and conversion processes in organic–inorganic halide perovskites. *ACS Energy Letters*, *2*(8), 1818–1824. https://doi.org/10.1021/acsenergylett.7b00437

[28] - Wang, S., Huang, Z., Wang, X., Li, Y., Günther, M., Valenzuela, S., Parikh, P., Cabreros, A., Xiong, W., & Meng, Y. S. (2018). Unveiling the role of TBP–litfsi complexes in perovskite solar cells. *Journal of the American Chemical Society*, *140*(48), 16720–16730. https://doi.org/10.1021/jacs.8b09809

[29] - Gao, K., Zhu, Z., Xu, B., Jo, S. B., Kan, Y., Peng, X., & Jen, A. K. Y. (2017). Highly efficient porphyrin-based OPV/perovskite hybrid solar cells with extended photoresponse and high fill factor. *Advanced Materials*, *29*(47), 1703980. https://doi.org/10.1002/adma.201703980

[30] - Schloemer, T. H., Christians, J. A., Luther, J. M., & Sellinger, A. (2019). Doping strategies for small molecule organic hole-transport materials: Impacts on perovskite solar cell performance and stability. *Chemical Science*, *10*(7), 1904–1935. https://doi.org/10.1039/c8sc05284k

[31] - Song, Z., Abate, A., Watthage, S. C., Liyanage, G. K., Phillips, A. B., Steiner, U., Graetzel, M., & Heben, M. J. (2016). In-situ observation of moisture-induced degradation of perovskite solar cells using laser-beam induced current. *2016 IEEE 43rd Photovoltaic Specialists Conference (PVSC)*. https://doi.org/10.1109/pvsc.2016.7749805

[32] - Song, S., Park, E. Y., Ma, B. S., Kim, D. J., Park, H. H., Kim, Y. Y., Shin, S. S., Jeon, N. J., Kim, T. S., & Seo, J. (2021). Selective defect passivation and topographical control of

4-dimethylaminopyridine at grain boundary for efficient and stable planar perovskite solar cells. *Advanced Energy Materials*, *11*(10), 2003382. https://doi.org/10.1002/aenm.202003382

[33] - Li, J., Gao, F., Wen, J., Xu, Z., Zhang, C., Hua, X., Cai, X., Li, Y., Shi, B., Han, Y., Ren, X., & Liu, S. (F. (2021). Effective surface passivation with 4-bromo-benzonitrile to enhance the performance of perovskite solar cells. *Journal of Materials Chemistry C*, *9*(47), 17089–17098. https://doi.org/10.1039/d1tc04615b

[34] - Liu, C., Yang, Y., Rakstys, K., Mahata, A., Franckevicius, M., Mosconi, E., Skackauskaite, R., Ding, B., Usiobo, O. J., Audinot, J.-N., Kanda, H., Driukas, S., Kavaliauskaite, G., Gulbinas, V., Dessimoz, M., Getautis, V., De Angelis, F., Ding, Y., Dai, S. Y., … Nazeeruddin, M. K. (2021). Tuning the structural isomers of phenylenediammonium cations to afford efficient and stable perovskite solar cells and modules. https://doi.org/10.21203/rs.3.rs-711763/v1

[35] - Chen, L.-M., Hong, Z., Li, G., & Yang, Y. (2009). Recent progress in polymer solar cells: Manipulation of polymer:fullerene morphology and the formation of efficient inverted polymer solar cells. *Advanced Materials*, *21*(14-15), 1434–1449. https://doi.org/10.1002/adma.200802854

[36] - Zuo, C., Bolink, H. J., Han, H., Huang, J., Cahen, D., & Ding, L. (2016). Advances in perovskite solar cells. *Advanced Science*, *3*(7), 1500324. https://doi.org/10.1002/advs.201500324

[37] - Jeng, J.-Y., Chiang, Y.-F., Lee, M.-H., Peng, S.-R., Guo, T.-F., Chen, P., & Wen, T.-C. (2013). Ch3NH3PBI3 perovskite/fullerene planar-heterojunction hybrid solar cells. *Advanced Materials*, *25*(27), 3727–3732. https://doi.org/10.1002/adma.201301327

[38] - Yang, X., Xi, J., Sun, Y., Zhang, Y., Zhou, G., & Wong, W.-Y. (2019). A dopant-free twisted organic small-molecule hole transport material for inverted planar perovskite solar cells with enhanced efficiency and operational stability. *Nano Energy*, *64*, 103946. https://doi.org/10.1016/j.nanoen.2019.103946

[39] - Pasquarelli, R. M., Ginley, D. S., & O'Hayre, R. (2011). Cheminform abstract: Solution processing of transparent conductors: From flask to film. *ChemInform*, *43*(2). https://doi.org/10.1002/chin.201202201

[40] - Im, J.-H., Kim, H.-S., & Park, N.-G. (2014). Morphology-photovoltaic property correlation in perovskite solar cells: One-step versus two-step deposition of CH3Nh3PBI3. *APL Materials*, *2*(8), 081510. https://doi.org/10.1063/1.4891275

[41] - Zhang, Y.-Y., Chen, S., Xu, P., Xiang, H., Gong, X.-G., Walsh, A., & Wei, S.-H. (2018). Intrinsic instability of the hybrid halide perovskite semiconductor CH3NH3PbI3*. *Chinese Physics Letters*, *35*(3), 036104. https://doi.org/10.1088/0256-307x/35/3/036104

[42] - El-Mellouhi, F., Marzouk, A., Bentria, E. T., Rashkeev, S. N., Kais, S., & Alharbi, F. H. (2016). Hydrogen bonding and stability of hybrid organic-inorganic perovskites. *ChemSusChem*, *9*(18), 2648–2655. https://doi.org/10.1002/cssc.201600864

[43] - Ruess, R., Benfer, F., Böcher, F., Stumpp, M., & Schlettwein, D. (2016). Stabilization of organic-inorganic perovskite layers by partial substitution of iodide by bromide in methylammonium lead iodide. *ChemPhysChem*, *17*(10), 1505–1511. https://doi.org/10.1002/cphc.201501168

[44] - Bischak, C. G., Hetherington, C. L., Wu, H., Aloni, S., Ogletree, D. F., Limmer, D. T., & Ginsberg, N. S. (2017). Origin of reversible photoinduced phase separation in hybrid perovskites. *Nano Letters*, *17*(2), 1028–1033. https://doi.org/10.1021/acs.nanolett.6b04453

[45] - Pereyra, C., Xie, H., & Lira-Cantu, M. (2021). Additive Engineering for stable halide perovskite solar cells. *Journal of Energy Chemistry*, *60*, 599–634. https://doi.org/10.1016/j.jechem.2021.01.037

[46] - Yan, W., Li, Y., Li, Y., Ye, S., Liu, Z., Wang, S., Bian, Z., & Huang, C. (2015). Stable high-performance hybrid perovskite solar cells with ultrathin polythiophene as hole-transporting layer. *Nano Research*, *8*(8), 2474–2480. https://doi.org/10.1007/s12274-015-0755-5

[47] - Xu, J., Voznyy, O., Comin, R., Gong, X., Walters, G., Liu, M., Kanjanaboos, P., Lan, X., & Sargent, E. H. (2016). Crosslinked remote-doped hole-extracting contacts enhance stability under accelerated lifetime testing in perovskite solar cells. *Advanced Materials*, *28*(14), 2807–2815. https://doi.org/10.1002/adma.201505630

[48] - Ameen, S., Rub, M. A., Kosa, S. A., Alamry, K. A., Akhtar, M. S., Shin, H.-S., Seo, H.-K., Asiri, A. M., & Nazeeruddin, M. K. (2015). Perovskite solar cells: Influence of hole transporting materials on power conversion efficiency. *ChemSusChem*, *9*(1), 10–27. https://doi.org/10.1002/cssc.201501228

[49] - Su, P.-Y., Huang, L.-B., Liu, J.-M., Chen, Y.-F., Xiao, L.-M., Kuang, D.-B., Mayor, M., & Su, C.-Y. (2017). A multifunctional poly-N-vinylcarbazole interlayer in perovskite solar cells for high stability and efficiency: A test with new triazatruxene-based hole transporting materials. *Journal of Materials Chemistry A*, *5*(5), 1913–1918. https://doi.org/10.1039/c6ta09314k

[50] - Ma, C., & Park, N.-G. (2020). Paradoxical approach with a hydrophilic passivation layer for moisture-stable, 23% efficient perovskite solar cells. *ACS Energy Letters*, *5*(10), 3268–3275. https://doi.org/10.1021/acsenergylett.0c01848

[51] - K H, G. (2021). Advances in surface passivation of perovskites using organic halide salts for efficient and stable solar cells. *Surfaces and Interfaces*, *26*, 101420. https://doi.org/10.1016/j.surfin.2021.101420

[52] - Lin, L., Jones, T. W., Yang, T. C. J., Duffy, N. W., Li, J., Zhao, L., Chi, B., Wang, X., & Wilson, G. J. (2020). Inorganic Electron Transport Materials in perovskite solar cells. *Advanced Functional Materials*, *31*(5), 2008300. https://doi.org/10.1002/adfm.202008300

[53] - Zhang, H., Ji, X., Yao, H., Fan, Q., Yu, B., & Li, J. (2022). Review on efficiency improvement effort of Perovskite Solar Cell. *Solar Energy*, *233*, 421–434. https://doi.org/10.1016/j.solener.2022.01.060

[54] - Ren, X., Liu, Y., Lee, D. G., Kim, W. B., Han, G. S., Jung, H. S., & Liu, S. (F. (2019). Chlorine-modified Sno 2 electron transport layer for high-efficiency perovskite solar cells. *InfoMat*, *2*(2), 401–408. https://doi.org/10.1002/inf2.12059

[55] - Roesch, R., Faber, T., von Hauff, E., Brown, T. M., Lira-Cantu, M., & Hoppe, H. (2015). Procedures and practices for evaluating thin-film solar cell stability. *Advanced Energy Materials*, *5*(20), 1501407. https://doi.org/10.1002/aenm.201501407

[56] - Leguy, A. M., Hu, Y., Campoy-Quiles, M., Alonso, M. I., Weber, O. J., Azarhoosh, P., van Schilfgaarde, M., Weller, M. T., Bein, T., Nelson, J., Docampo, P., & Barnes, P. R. (2015). Reversible hydration of CH3Nh3PBI3 in films, single crystals, and Solar Cells. *Chemistry of Materials*, *27*(9), 3397–3407. https://doi.org/10.1021/acs.chemmater.5b00660

[57] - Philippe, B., Park, B.-W., Lindblad, R., Oscarsson, J., Ahmadi, S., Johansson, E. M., & Rensmo, H. (2015). Chemical and electronic structure characterization of lead halide perovskites and stability behavior under different exposures—a photoelectron spectroscopy investigation. *Chemistry of Materials*, *27*(5), 1720–1731. https://doi.org/10.1021/acs.chemmater.5b00348

[58] - Xiao, Z., Yuan, Y., Shao, Y., Wang, Q., Dong, Q., Bi, C., Sharma, P., Gruverman, A., & Huang, J. (2014). Giant switchable photovoltaic effect in organometal trihalide perovskite devices. *Nature Materials*, *14*(2), 193–198. https://doi.org/10.1038/nmat4150

[59] - Merdasa, A., Bag, M., Tian, Y., Källman, E., Dobrovolsky, A., & Scheblykin, I. G. (2016). Super-resolution luminescence microspectroscopy reveals the mechanism of photoinduced degradation in CH3nh3PBI3 perovskite nanocrystals. *The Journal of Physical Chemistry C*, *120*(19), 10711–10719. https://doi.org/10.1021/acs.jpcc.6b03512

[60] - Li, B., Li, Y., Zheng, C., Gao, D., & Huang, W. (2016). Advancements in the stability of perovskite solar cells: Degradation mechanisms and improvement approaches. *RSC Advances*, *6*(44), 38079–38091. https://doi.org/10.1039/c5ra27424a

[61] - Wu, C.-G., Chiang, C.-H., Tseng, Z.-L., Nazeeruddin, M. K., Hagfeldt, A., & Grätzel, M. (2015). High efficiency stable inverted perovskite solar cells without current hysteresis. *Energy & Environmental Science*, *8*(9), 2725–2733. https://doi.org/10.1039/c5ee00645g

[62] - You, J., Yang, Y. (M., Hong, Z., Song, T.-B., Meng, L., Liu, Y., Jiang, C., Zhou, H., Chang, W.-H., Li, G., & Yang, Y. (2014). Moisture assisted perovskite film growth for

High Performance Solar Cells. *Applied Physics Letters*, *105*(18), 183902. https://doi.org/10.1063/1.4901510

[63] - Wang, Q., Chen, B., Liu, Y., Deng, Y., Bai, Y., Dong, Q., & Huang, J. (2017). Scaling behavior of moisture-induced grain degradation in polycrystalline hybrid perovskite thin films. *Energy & Environmental Science*, *10*(2), 516–522. https://doi.org/10.1039/c6ee02941h

[64] - Niu, G., Li, W., Meng, F., Wang, L., Dong, H., & Qiu, Y. (2014). Study on the stability of CH3Nh3PBI3films and the effect of post-modification by aluminum oxide in all-solid-state hybrid solar cells. *J. Mater. Chem. A*, *2*(3), 705–710. https://doi.org/10.1039/c3ta13606j

[65] - Yang, J., Siempelkamp, B. D., Liu, D., & Kelly, T. L. (2015). Investigation of CH3nh3PBI3 degradation rates and mechanisms in controlled humidity environments using *in situ* techniques. *ACS Nano*, *9*(2), 1955–1963. https://doi.org/10.1021/nn506864k

[66] - Aristidou, N., Sanchez-Molina, I., Chotchuangchutchaval, T., Brown, M., Martinez, L., Rath, T., & Haque, S. A. (2015). The role of oxygen in the degradation of methylammonium lead trihalide perovskite photoactive layers. *Angewandte Chemie International Edition*, *54*(28), 8208–8212. https://doi.org/10.1002/anie.201503153

[67] - Bryant, D., Aristidou, N., Pont, S., Sanchez-Molina, I., Chotchunangatchaval, T., Wheeler, S., Durrant, J. R., & Haque, S. A. (2016). Light and oxygen induced degradation limits the operational stability of methylammonium lead triiodide perovskite solar cells. *Energy & Environmental Science*, *9*(5), 1655–1660. https://doi.org/10.1039/c6ee00409a

[68] - Sun, Q., Fassl, P., Becker-Koch, D., Bausch, A., Rivkin, B., Bai, S., Hopkinson, P. E., Snaith, H. J., & Vaynzof, Y. (2017). Role of microstructure in oxygen induced photodegradation of methylammonium lead triiodide perovskite films. *Advanced Energy Materials*, *7*(20), 1700977. https://doi.org/10.1002/aenm.201700977

[69] - Unger, E. L., Hoke, E. T., Bailie, C. D., Nguyen, W. H., Bowring, A. R., Heumüller, T., Christoforo, M. G., & McGehee, M. D. (2014). Hysteresis and transient behavior in current–voltage measurements of hybrid-perovskite absorber solar cells. *Energy Environ. Sci.*, *7*(11), 3690–3698. https://doi.org/10.1039/c4ee02465f

[70] - Schmidt, T. M., Larsen-Olsen, T. T., Carlé, J. E., Angmo, D., & Krebs, F. C. (2015). Upscaling of perovskite solar cells: Fully ambient roll processing of flexible perovskite solar cells with printed back electrodes. *Advanced Energy Materials*, *5*(15), 1500569. https://doi.org/10.1002/aenm.201500569

[71] - Stranks, S. D., Eperon, G. E., Grancini, G., Menelaou, C., Alcocer, M. J., Leijtens, T., Herz, L. M., Petrozza, A., & Snaith, H. J. (2013). Electron-hole diffusion lengths exceeding 1 micrometer in an organometal trihalide perovskite absorber. *Science*, *342*(6156), 341–344. https://doi.org/10.1126/science.1243982

[72] - Marinova, N., Tress, W., Humphry-Baker, R., Dar, M. I., Bojinov, V., Zakeeruddin, S. M., Nazeeruddin, M. K., & Grätzel, M. (2015). Light harvesting and charge recombination in CH3nh3PBI3 perovskite solar cells studied by hole transport layer thickness variation. *ACS Nano*, *9*(4), 4200–4209. https://doi.org/10.1021/acsnano.5b00447

[73] - Herz, L. M. (2017). Charge-carrier mobilities in metal halide perovskites: Fundamental mechanisms and limits. *ACS Energy Letters*, *2*(7), 1539–1548. https://doi.org/10.1021/acsenergylett.7b00276

[74] - Amat, A., Mosconi, E., Ronca, E., Quarti, C., Umari, P., Nazeeruddin, M. K., Grätzel, M., & De Angelis, F. (2014). Cation-induced band-gap tuning in organohalide perovskites: Interplay of spin–orbit coupling and octahedra tilting. *Nano Letters*, *14*(6), 3608–3616. https://doi.org/10.1021/nl5012992

[75] - Prochowicz, D., Tavakoli, M. M., Wolska-Pietkiewicz, M., Jędrzejewska, M., Trivedi, S., Kumar, M., Zakeeruddin, S. M., Lewiński, J., Graetzel, M., & Yadav, P. (2020). Suppressing recombination in perovskite solar cells via surface engineering of TiO2 ETL. *Solar Energy*, *197*, 50–57. https://doi.org/10.1016/j.solener.2019.12.070

[76] - Tress, W., Marinova, N., Moehl, T., Zakeeruddin, S. M., Nazeeruddin, M. K., & Grätzel, M. (2015). Understanding the rate-dependent J–V hysteresis, slow time component, and aging in CH3nh3PBI3 perovskite solar cells: The role of a compensated electric field. *Energy & Environmental Science*, *8*(3), 995–1004. https://doi.org/10.1039/c4ee03664f

[77] - Hang, P., Xie, J., Kan, C., Li, B., Zhang, Y., Gao, P., Yang, D., & Yu, X. (2021). Stabilizing Fullerene for burn-in-free and stable perovskite solar cells under ultraviolet preconditioning and light soaking. *Advanced Materials*, *33*(10), 2006910. https://doi.org/10.1002/adma.202006910

[78] - Bu, T., Li, J., Zheng, F., Chen, W., Wen, X., Ku, Z., Peng, Y., Zhong, J., Cheng, Y.-B., & Huang, F. (2018). Universal passivation strategy to slot-die printed SnO_2 for hysteresis-free efficient flexible perovskite solar module. *Nature Communications*, *9*(1). https://doi.org/10.1038/s41467-018-07099-9

[79] - Chen, J., Kim, S.-G., & Park, N.-G. (2018). FA0.88cs0.12PBI3− *x* (PF6) *x* interlayer formed by Ion Exchange reaction between perovskite and hole transporting layer for improving photovoltaic performance and stability. *Advanced Materials*, *30*(40), 1801948. https://doi.org/10.1002/adma.201801948

[80] - Liu, Z., Qiu, L., Ono, L. K., He, S., Hu, Z., Jiang, M., Tong, G., Wu, Z., Jiang, Y., Son, D.-Y., Dang, Y., Kazaoui, S., & Qi, Y. (2020). A holistic approach to interface stabilization for efficient perovskite solar modules with over 2,000-hour operational stability. *Nature Energy*, *5*(8), 596–604. https://doi.org/10.1038/s41560-020-0653-2

[81] - Ke, W., Fang, G., Liu, Q., Xiong, L., Qin, P., Tao, H., Wang, J., Lei, H., Li, B., Wan, J., Yang, G., & Yan, Y. (2015). Low-temperature solution-processed tin oxide as an

alternative electron transporting layer for efficient perovskite solar cells. *Journal of the American Chemical Society*, *137*(21), 6730–6733. https://doi.org/10.1021/jacs.5b01994

[82] - You, S., Zeng, H., Ku, Z., Wang, X., Wang, Z., Rong, Y., Zhao, Y., Zheng, X., Luo, L., Li, L., Zhang, S., Li, M., Gao, X., & Li, X. (2020). Multifunctional polymer-regulated SnO2 nanocrystals enhance interface contact for efficient and stable planar perovskite solar cells. *Advanced Materials*, *32*(43), 2003990. https://doi.org/10.1002/adma.202003990

[83] - Jiang, Q., Zhang, X., & You, J. (2018). SnO2: A wonderful electron transport layer for perovskite solar cells. *Small*, *14*(31), 1801154. https://doi.org/10.1002/smll.201801154

[84] - Tao, J., Liu, X., Shen, J., Wang, H., Xue, J., Su, C., Guo, H., Fu, G., Kong, W., & Yang, S. (2022). Functionalized SnO2 films by using EDTA-2 m for high efficiency perovskite solar cells with efficiency over 23%. *Chemical Engineering Journal*, *430*, 132683. https://doi.org/10.1016/j.cej.2021.132683

[85] - Yoo, J. J., Seo, G., Chua, M. R., Park, T. G., Lu, Y., Rotermund, F., Kim, Y.-K., Moon, C. S., Jeon, N. J., Correa-Baena, J.-P., Bulović, V., Shin, S. S., Bawendi, M. G., & Seo, J. (2021). Efficient perovskite solar cells via improved carrier management. *Nature*, *590*(7847), 587–593. https://doi.org/10.1038/s41586-021-03285-w

[86] - Gaur, R., Roy, S., Kallem, P., & Banat, F. (2022). Experimental and theoretical investigation of hydrogen bonded supramolecular assemblies through water molecules in a copper(ii)-egta complex. *Journal of Molecular Structure*, *1265*, 133400. https://doi.org/10.1016/j.molstruc.2022.133400

[87] - Gaur, R. (2019). Ionic nature of cadmium polymer plays decisive role in selective dye adsorption. *Journal of Solid State Chemistry*, *278*, 120907. https://doi.org/10.1016/j.jssc.2019.120907

[88] - Gaur, R., Susmitha, A., Chary, K. V., & Mishra, L. (2014). A water soluble calcium–sodium based coordination polymer: Selective release of calcium at specific binding sites on proteins. *RSC Adv.*, *4*(46), 24038–24041. https://doi.org/10.1039/c4ra01005a

[89] - Gaur, R. (2019). Selective anionic dye adsorption, topology and luminescence study of structurally diverse cadmium(ii) coordination polymers. *Inorganic Chemistry Frontiers*, *6*(1), 278–286. https://doi.org/10.1039/c8qi01039k

[90] - Gundrizer, T. A., & Davydov, A. A. (1975). IR spectra of oxygen adsorbed on SnO2. *Reaction Kinetics and Catalysis Letters*, *3*(1), 63–70. https://doi.org/10.1007/bf02216890

[91] - Yang, D., Zhou, L., Yu, W., Zhang, J., & Li, C. (2014). Work-function-tunable chlorinated graphene oxide as an anode interface layer in high-efficiency polymer solar cells. *Advanced Energy Materials*, *4*(15), 1400591. https://doi.org/10.1002/aenm.201400591

[92] - Choi, K., Lee, J., Kim, H. I., Park, C. W., Kim, G.-W., Choi, H., Park, S., Park, S. A., & Park, T. (2018). Thermally stable, planar hybrid perovskite solar cells with high efficiency. *Energy & Environmental Science*, *11*(11), 3238–3247. https://doi.org/10.1039/c8ee02242a

[93] - Sun, Y., Zhang, J., Yu, H., Wang, J., Huang, C., & Huang, J. (2021). Mechanism of bifunctional P-amino benzenesulfonic acid modified interface in perovskite solar cells. *Chemical Engineering Journal*, *420*, 129579. https://doi.org/10.1016/j.cej.2021.129579

[94] - Yang, D., Yang, R., Wang, K., Wu, C., Zhu, X., Feng, J., Ren, X., Fang, G., Priya, S., & Liu, S. (2018). High efficiency planar-type perovskite solar cells with negligible hysteresis using EDTA-complexed SnO2. *Nature Communications*, *9*(1). https://doi.org/10.1038/s41467-018-05760-x

[95] - Du, T., Burgess, C. H., Kim, J., Zhang, J., Durrant, J. R., & McLachlan, M. A. (2017). Formation, location and beneficial role of PBI2 in lead halide perovskite solar cells. *Sustainable Energy & Fuels*, *1*(1), 119–126. https://doi.org/10.1039/c6se00029k

[96] - Chen, B., Rudd, P. N., Yang, S., Yuan, Y., & Huang, J. (2019). Imperfections and their passivation in halide perovskite solar cells. *Chemical Society Reviews*, *48*(14), 3842–3867. https://doi.org/10.1039/c8cs00853a

[97] - Thakur, U., Kwon, U., Hasan, M. M., Yin, W., Kim, D., Ha, N. Y., Lee, S., Ahn, T. K., & Park, H. J. (2017). Erratum: Corrigendum: Investigation into the advantages of pure perovskite film without PBI2 for high performance solar cell. *Scientific Reports*, *7*(1). https://doi.org/10.1038/srep43979

[98] - Liu, Y., Sun, J., Yang, Z., Yang, D., Ren, X., Xu, H., Yang, Z., & Liu, S. F. (2016). 20-mm-large single-crystalline formamidinium-perovskite wafer for mass production of integrated photodetectors. *Advanced Optical Materials*, *4*(11), 1829–1837. https://doi.org/10.1002/adom.201600327

[99] - Chen, B., Yang, M., Zheng, X., Wu, C., Li, W., Yan, Y., Bisquert, J., Garcia-Belmonte, G., Zhu, K., & Priya, S. (2015). Impact of capacitive effect and Ion Migration on the hysteretic behavior of perovskite solar cells. *The Journal of Physical Chemistry Letters*, *6*(23), 4693–4700. https://doi.org/10.1021/acs.jpclett.5b02229

[100] - Green, M. A., Ho-Baillie, A., & Snaith, H. J. (2014). The emergence of perovskite solar cells. *Nature Photonics*, *8*(7), 506–514. https://doi.org/10.1038/nphoton.2014.134

[101] - Wetzelaer, G.-J. A., Scheepers, M., Sempere, A. M., Momblona, C., Ávila, J., & Bolink, H. J. (2015). Trap-assisted non-radiative recombination in organic-inorganic perovskite solar cells. *Advanced Materials*, *27*(11), 1837–1841. https://doi.org/10.1002/adma.201405372

[102] - Ono, L. K., Liu, S. (F., & Qi, Y. (2020). Reducing detrimental defects for high-performance metal halide perovskite solar cells. *Angewandte Chemie International Edition*, *59*(17), 6676–6698. https://doi.org/10.1002/anie.201905521

[103] - Wang, S., Wang, A., Deng, X., Xie, L., Xiao, A., Li, C., Xiang, Y., Li, T., Ding, L., & Hao, F. (2020). Lewis acid/base approach for efficacious defect passivation in perovskite solar cells. *Journal of Materials Chemistry A*, *8*(25), 12201–12225. https://doi.org/10.1039/d0ta03957h

[104] - Gao, F., Zhao, Y., Zhang, X., & You, J. (2019). Recent progresses on defect passivation toward efficient perovskite solar cells. *Advanced Energy Materials*, *10*(13), 1902650. https://doi.org/10.1002/aenm.201902650

[105] - Wang, F., Bai, S., Tress, W., Hagfeldt, A., & Gao, F. (2018). Defects engineering for high-performance perovskite solar cells. *Npj Flexible Electronics*, *2*(1). https://doi.org/10.1038/s41528-018-0035-z

[106] - Ball, J. M., & Petrozza, A. (2016). Defects in perovskite-halides and their effects in solar cells. *Nature Energy*, *1*(11). https://doi.org/10.1038/nenergy.2016.149

[107] - Du, M., Zhu, X., Wang, L., Wang, H., Feng, J., Jiang, X., Cao, Y., Sun, Y., Duan, L., Jiao, Y., Wang, K., Ren, X., Yan, Z., Pang, S., & Liu, S. (F. (2020). High-pressure nitrogen-extraction and effective passivation to attain highest large-area perovskite solar module efficiency. *Advanced Materials*, *32*(47), 2004979. https://doi.org/10.1002/adma.202004979

[108] - Zhang, F., & Zhu, K. (2019). Additive Engineering for efficient and stable perovskite solar cells. *Advanced Energy Materials*, *10*(13), 1902579. https://doi.org/10.1002/aenm.201902579

[109] - Xiong, S., Hao, T., Sun, Y., Yang, J., Ma, R., Wang, J., Gong, S., Liu, X., Ding, L., Fahlman, M., & Bao, Q. (2021). Defect passivation by nontoxic biomaterial yields 21% efficiency perovskite solar cells. *Journal of Energy Chemistry*, *55*, 265–271. https://doi.org/10.1016/j.jechem.2020.06.061

[110] - Liu, C., Yang, Y., Rakstys, K., Mahata, A., Franckevicius, M., Mosconi, E., Skackauskaite, R., Ding, B., Brooks, K. G., Usiobo, O. J., Audinot, J.-N., Kanda, H., Driukas, S., Kavaliauskaite, G., Gulbinas, V., Dessimoz, M., Getautis, V., De Angelis, F., Ding, Y., … Nazeeruddin, M. K. (2021). Tuning structural isomers of phenylenediammonium to afford efficient and stable perovskite solar cells and modules. *Nature Communications*, *12*(1). https://doi.org/10.1038/s41467-021-26754-2

[111] - Cai, W., Wang, Y., Shang, W., Liu, J., Wang, M., Dong, Q., Han, Y., Li, W., Ma, H., Wang, P., Guo, J., & Shi, Y. (2022). Lewis base governing superfacial Proton Behavior of hybrid perovskite: Basicity dependent passivation strategy. *Chemical Engineering Journal*, *446*, 137033. https://doi.org/10.1016/j.cej.2022.137033

[112] - Huang, L.-B., Su, P.-Y., Liu, J.-M., Huang, J.-F., Chen, Y.-F., Qin, S., Guo, J., Xu, Y.-W., & Su, C.-Y. (2018). Interface Engineering of perovskite solar cells with multifunctional polymer interlayer toward improved performance and stability. *Journal of Power Sources*, *378*, 483–490. https://doi.org/10.1016/j.jpowsour.2017.12.082

[113] - Fairfield, D. J., Sai, H., Narayanan, A., Passarelli, J. V., Chen, M., Palasz, J., Palmer, L. C., Wasielewski, M. R., & Stupp, S. I. (2019). Structure and chemical stability in perovskite–polymer hybrid photovoltaic materials. *Journal of Materials Chemistry A*, *7*(4), 1687–1699. https://doi.org/10.1039/c8ta07545j

[114] - Li, M., Yan, X., Kang, Z., Huan, Y., Li, Y., Zhang, R., & Zhang, Y. (2018). Hydrophobic polystyrene passivation layer for simultaneously improved efficiency and stability in perovskite solar cells. *ACS Applied Materials & Interfaces*, *10*(22), 18787–18795. https://doi.org/10.1021/acsami.8b04776

[115] - Cai, F., Cai, J., Yang, L., Li, W., Gurney, R. S., Yi, H., Iraqi, A., Liu, D., & Wang, T. (2018). Molecular engineering of conjugated polymers for efficient hole transport and defect passivation in perovskite solar cells. *Nano Energy*, *45*, 28–36. https://doi.org/10.1016/j.nanoen.2017.12.028

[116] - Zhu, H., Liu, Y., Eickemeyer, F. T., Pan, L., Ren, D., Ruiz-Preciado, M. A., Carlsen, B., Yang, B., Dong, X., Wang, Z., Liu, H., Wang, S., Zakeeruddin, S. M., Hagfeldt, A., Dar, M. I., Li, X., & Grätzel, M. (2020). Tailored amphiphilic molecular mitigators for stable perovskite solar cells with 23.5% efficiency. *Advanced Materials*, *32*(12), 1907757. https://doi.org/10.1002/adma.201907757

[117] - Zha, W., Chen, F., Yang, D., Shen, Q., & Zhang, L. (2018). High-performance LI6.4La3Zr1.4Ta0.6O12/Poly(ethylene oxide)/succinonitrile composite electrolyte for solid-state lithium batteries. *Journal of Power Sources*, *397*, 87–94. https://doi.org/10.1016/j.jpowsour.2018.07.005

[118] - Bi, J., Mu, D., Wu, B., Fu, J., Yang, H., Mu, G., Zhang, L., & Wu, F. (2020). A hybrid solid electrolyte li0.33La0.557Tio3/poly(acylonitrile) membrane infiltrated with a succinonitrile-based electrolyte for solid state lithium-ion batteries. *Journal of Materials Chemistry A*, *8*(2), 706–713. https://doi.org/10.1039/c9ta08601c

[119] - Yang, X., Ni, Y., Zhang, Y., Wang, Y., Yang, W., Luo, D., Tu, Y., Gong, Q., Yu, H., & Zhu, R. (2021). Multiple-defect management for efficient perovskite photovoltaics. *ACS Energy Letters*, *6*(7), 2404–2412. https://doi.org/10.1021/acsenergylett.1c01039

[120] - Roose, B., Dey, K., Chiang, Y.-H., Friend, R. H., & Stranks, S. D. (2020). Critical assessment of the use of excess lead iodide in lead halide perovskite solar cells. *The Journal of Physical Chemistry Letters*, *11*(16), 6505–6512. https://doi.org/10.1021/acs.jpclett.0c01820

[121] - Radicchi, E., Mosconi, E., Elisei, F., Nunzi, F., & De Angelis, F. (2019). Understanding the solution chemistry of lead halide perovskites precursors. *ACS Applied Energy Materials*, *2*(5), 3400–3409. https://doi.org/10.1021/acsaem.9b00206

[122] - Manser, J. S., Saidaminov, M. I., Christians, J. A., Bakr, O. M., & Kamat, P. V. (2016). Making and breaking of lead halide perovskites. *Accounts of Chemical Research*, *49*(2), 330–338. https://doi.org/10.1021/acs.accounts.5b00455

[123] - Li, X., Bi, D., Yi, C., Décoppet, J.-D., Luo, J., Zakeeruddin, S. M., Hagfeldt, A., & Grätzel, M. (2016). A vacuum flash–assisted solution process for high-efficiency large-area perovskite solar cells. *Science*, *353*(6294), 58–62. https://doi.org/10.1126/science.aaf8060

[124] - Noel, N. K., Abate, A., Stranks, S. D., Parrott, E. S., Burlakov, V. M., Goriely, A., & Snaith, H. J. (2014). Enhanced photoluminescence and solar cell performance *via* lewis base passivation of organic–inorganic lead halide perovskites. *ACS Nano*, *8*(10), 9815–9821. https://doi.org/10.1021/nn5036476

[125] - Yang, W., Ling, B., Hu, B., Yin, H., Mao, J., & Walsh, P. J. (2019). Inside cover: Synergistic n-heterocyclic carbene/palladium-catalyzed umpolung 1,4-addition of aryl iodides to enals (angew. chem. int. Ed. 1/2020). *Angewandte Chemie International Edition*, *59*(1), 2–2. https://doi.org/10.1002/anie.201914768

[126] - Ren, X., Yang, D., Yang, Z., Feng, J., Zhu, X., Niu, J., Liu, Y., Zhao, W., & Liu, S. F. (2017). Solution-processed Nb:SnO2 electron transport layer for efficient planar perovskite solar cells. *ACS Applied Materials & Interfaces*, *9*(3), 2421–2429. https://doi.org/10.1021/acsami.6b13362

[127] - Niu, T., Lu, J., Jia, X., Xu, Z., Tang, M.-C., Barrit, D., Yuan, N., Ding, J., Zhang, X., Fan, Y., Luo, T., Zhang, Y., Smilgies, D.-M., Liu, Z., Amassian, A., Jin, S., Zhao, K., & Liu, S. (2019). Interfacial Engineering at the 2D/3D heterojunction for high-performance perovskite solar cells. *Nano Letters*, *19*(10), 7181–7190. https://doi.org/10.1021/acs.nanolett.9b02781

[128] - Ren, X., Xie, L., Kim, W. B., Lee, D. G., Jung, H. S., & Liu, S. (F. (2019). Chemical bath deposition of CO-doped Tio 2 electron transport layer for hysteresis-suppressed high-efficiency planar perovskite solar cells. *Solar RRL*, *3*(9), 1900176. https://doi.org/10.1002/solr.201900176

[129] - Shi, D., Adinolfi, V., Comin, R., Yuan, M., Alarousu, E., Buin, A., Chen, Y., Hoogland, S., Rothenberger, A., Katsiev, K., Losovyj, Y., Zhang, X., Dowben, P. A., Mohammed, O. F., Sargent, E. H., & Bakr, O. M. (2015). Low trap-state density and long carrier diffusion in organolead trihalide perovskite single crystals. *Science*, *347*(6221), 519–522. https://doi.org/10.1126/science.aaa2725

[130] - Ginting, R. T., Jeon, M.-K., Lee, K.-J., Jin, W.-Y., Kim, T.-W., & Kang, J.-W. (2017). Degradation mechanism of planar-perovskite solar cells: Correlating evolution of iodine distribution and photocurrent hysteresis. *Journal of Materials Chemistry A, 5*(9), 4527–4534. https://doi.org/10.1039/c6ta09202k